

Manuscript version: Author's Accepted Manuscript

The version presented in WRAP is the author's accepted manuscript and may differ from the published version or Version of Record.

Persistent WRAP URL:

<http://wrap.warwick.ac.uk/153055>

How to cite:

Please refer to published version for the most recent bibliographic citation information. If a published version is known of, the repository item page linked to above, will contain details on accessing it.

Copyright and reuse:

The Warwick Research Archive Portal (WRAP) makes this work by researchers of the University of Warwick available open access under the following conditions.

© 2021 Elsevier. Licensed under the Creative Commons Attribution-NonCommercial-NoDerivatives 4.0 International <http://creativecommons.org/licenses/by-nc-nd/4.0/>.



Publisher's statement:

Please refer to the repository item page, publisher's statement section, for further information.

For more information, please contact the WRAP Team at: wrap@warwick.ac.uk.

Laser Wobble Welding of Fluid-based Cooling Channel Joining for Battery Thermal Management

Nikhil Kumar^{1,*}, Abhishek Das¹, Tom Dale², Iain Masters¹

¹WMG, The University of Warwick, Coventry CV4 7AL, UK

²Nobel Automotive, Coventry CV34 6NJ, UK

*Corresponding author: nikhil.kumar@warwick.ac.uk

Abstract

Aluminium alloys are increasingly used to fabricate cooling channels for the thermal management of Li-ion batteries. Cooling channel fabrication involves a number of manufacturing operations including material extrusion, forming and joining/welding. In general, welding of aluminium alloys is challenging as they are both highly reflective and thermally conductive. To address the joining challenges, this paper is focused on developing an optimised joining process to connect a thin, flanged cooling channel to the thick module manifold of the battery thermal management system to create a watertight joint with high mechanical strength. As continuous seam welding was required, laser welding was the preferred as it is a non-contact process combining high speed and precision. For this application, 0.4 mm Al cooling channel was welded with 1.5 mm Al endplate/module manifold using a wobble head integrated with 1 kW CW fibre laser system. The effect of process parameters including line energy, incident angle, laser power, welding speed and beam offset were investigated to optimise both the weld geometry and strength. Microstructure, micro-hardness and grain formation analyses were carried out to understand the metallurgical behaviour of the weld. Beam offset had the most significant effect on the responses such as weld strength, throat thickness and modified throat thickness, and laser power had a significant influence on two key geometric features of the fusion zone, i.e. penetration depth and weld width. Weld strength was optimised using a developed surrogate model and a maximum load of 646.89 N was achieved using 0.2 mm beam offset, 331.82 W laser power and 659.10 mm/min welding speed. Using this optimum combination, a leak-proof cooling channel and module manifold joint were produced for battery thermal management.

Keywords: Cooling channel, Li-ion battery, Laser welding, Beam offset, Optimisation;

1. Introduction

The energy sector has been changing in the past few years, driven by the transition toward renewable energies. Storage systems are essential for the energy supply to the devices. Based on the energy requirements, these energy storage systems may consist of a large number of battery cells. For example, a battery pack for an electric automotive vehicle comprises of hundreds or thousands of battery cells to deliver the required power and driving ranges [1]. The battery cells are assembled in modules and several battery modules are connected to form a battery pack. To manufacture a battery module, a number of material connections are required, e.g. electrical joining requirements including tab to cell terminal or tab to busbar connections; and structural joining requirements including cooling channel fabrication, battery can sealing, or battery pack encasing. Therefore, these joints can be broadly classified into two main categories: *electrical connection* and *structural connection*.

To make a satisfactory *electrical connection*, several research studies have been reported in the literature addressing the mechanical, metallurgical, electrical and thermal requirements of these electrical joints. Das, et al. [1] reviewed the applicability of the major and emerging joining techniques for battery pack manufacturing. They identified the advantages, disadvantages, limitations and concerns for various joining technologies based on battery pack construction and connectivity requirements for the dominant cell types in use. Brand, et al. [2] also presented a comprehensive overview of joining battery cells by resistance spot, ultrasonic and laser beam welding. They found that the lowest electrical contact resistances and the highest joint strengths were obtained with laser beam welding because the optimal weld geometry could be realized. Schmidt, et al. [3] investigated the joining of lithium-ion batteries using laser beam welding. According to the electrical connection, the following material combinations need to be joined within a pouch cell-based battery module: Al/Al, Cu/Cu for parallel circuits and Al/Cu for series circuits. Similarly, the *structural connection* within the battery module is important to achieve the desired functionality of the battery module. For example, temperature control of the battery module is vital for smooth operation, durability and improved safety in battery-powered electric vehicles. One method of maintaining the module temperature within the battery operating range (i.e. 15°C to 35°C) [4], is to pass cooling fluid through channels placed between battery cells and connected to the module manifold [5]. As the cooling system is liquid-based, the joints must be both leak-proof and strong. Laser welding has several advantages compared to conventional welding processes (ultrasonic welding, resistance welding, pulsed-TIG etc.) making it suitable for producing leak-proof connections. Laser

welding was widely studied for different types of joints such as overlap, butt and T-joint configurations [58-62]. Laser overlap welding has various applications in the field of the automotive industry like door entry, triangle window, A-pillar, roof tail, etc. Whereas, laser butt-welding is used for welding tubes in roll-forming production lines as an alternative method for high frequency induction welding and T-joints are normally used for double-sided laser welding of skin-stringer for producing defect-free welds [62]. Laser welding is a non-contact joining process. The localized and narrow heat zone can create a high-quality weld such that common re-working and after-work procedures are no-longer required. Additionally, the laser wobbling/oscillation technique is suitable for joining highly reflecting and conducting materials used in battery connections as well as for producing structural seam weld. Laser welding is an attractive process to industry due to its ease of automation, high processing speed, high repeatability and cost-effective process [6, 7].

Kraetzsch, et al. [8] studied laser beam welding (fibre laser) with high-frequency beam oscillation for dissimilar materials (Al/Cu) joining. They concluded that the fibre laser and the use of high speed scanning head with power modulation offers possibilities for crack free welding of dissimilar metals. Shah et al. [56] and Khodabakhshi et al. [57] were studied the effect of beam wobbling (circular) on laser welding of aluminium and magnesium alloy with nickel interlayer. They have found that the laser beam wobble enhanced the joint quality by widening the bond area (interlayer waist) and mitigating brittle lower weld zone formation in the region. Whilst, fracture occurred when linear laser beam welding was used due to the presence of brittle lower weld zone in the region. In the research of Das et al. [9], the feasibility of producing fillet edge welds, using the wobble (circular) technique, to join 0.3 mm thin aluminium to 1.5 mm thick aluminium sheet were investigated. They have concluded that the laser power had the significant influence on both the penetration depth and weld width. Also, the penetration depth and weld width were decreased with increasing welding speed due to the reduction in heat input per unit area. Shannon and Chen [10] studied the laser welding of aluminium and copper for battery welding applications using a 500 W single-mode fibre laser. They concluded that the lap weld geometry (tab welding application) appears well-aligned to take advantage of the single-mode fibre laser for high volume pack manufacture. These studies were mainly focused on the electrical connections within the battery module. However, the application of laser welding to produce leak-proof joints between the cooling channels and the module manifold of a battery cooling system not explored in a comprehensive way.

A number of approaches are being examined by researchers for cooling lithium-ion battery modules using different coolants such as air, mineral oil, water, and phase change material [4, 5, 11-13]. Liquid-based cooling systems have received the most attention, with water-based coolant having outstanding thermal properties and low cost [4, 11]. Several investigations have been conducted to improve the quality of cooling systems through the use of simulations, cooling channel design, mass flow rate optimisation, inlet temperature variation, or an optimum number of cooling channels. Design and fabrication processes are interrelated and are to be addressed simultaneously. Therefore, in this paper, the joining of cooling channel using laser welding process was conducted, which can be used/helpful for another cooling channel design/joining application.

Wang, et al. [5] developed an integrated cooling system combining a forced internal gas cooling circuit and a liquid cooling plate to overcome heating in Li-ion batteries. They have concluded that the temperature consistency of cells could be enhanced significantly with this integrated cooling method. In the work of Patil, et al. [12], it was concluded that the cooling energy efficiency of lithium-ion pouch cells was enhanced with low inlet coolant temperature, low inlet coolant mass flow rate and a high number of cooling channels. Ye, et al. [13] also studied the design and optimization of the cooling plate for the battery module of an electric vehicle and found that the battery temperature difference and the pressure drop decreased when the cross-section and number of coolant channels were increased whilst holding the inlet coolant flow rate constant [14]. However, the joining aspects for manufacturing these cooling channels are not addressed properly. Joining/sealing techniques were adopted for the joining of the cooling channel to the module manifold in [15-17] which may produce leakage of cooling fluid. Therefore, this paper explores, for the first time, to optimise the laser welding process parameters, based on experimental investigations for joining the cooling channel and module manifold of battery cooling system, to obtain watertight joints with high mechanical strength. The reported literature on the joining requirements within a battery module assembly is given in **Table 1** showing that the research work has mainly focused on the electrical rather than the structural requirements and identified the research gap. Within the scope of the literature review, it has been observed that the highest joint strengths can be obtained with laser beam welding [2, 3]. Although the wobble technique has been more commonly used in the literature for overlap joints [2, 3, 56, 57], it was used in this study to produce fillet edge joints which considered more suitable for sealing applications [9] and obviated the need for additional filler material.

Table 1. Review on joining requirements within battery module

| Joining requirements | Joining within Battery module assembly | | |
|----------------------|---|---|--|
| | Electrical joint | Structural joint | |
| | | Battery casing | Fluid connection |
| Solid state welding | Brand, et al. [2] Tagawa and Brodd [18] Berdichevsky, et al. [19] Das, et al. [20], [21] Shawn Lee, et al. [22] Dhara and Das [23] Reinhart, et al. [24] Das, et al. [25] Ma and Zhang [26] | Buck, et al. [15] Kuruma and Inoue [16] | Buck, et al. [15] Kuruma and Inoue [16] Chu, et al. [17] |
| Fusion welding | Brand, et al. [2] Schmidt, et al. [3] Shannon and Chen [10] Tagawa and Brodd [18] Walter, et al. [27] Shannon [28] Shaikh, et al. [29] Dong, et al. [30] Das, et al. [21], [31] | Shannon and Chen [10] Sun, et al. [32] Das, et al. [33] | <i>To be addressed in this paper</i> |

The laser process parameters were optimised in two stages. Firstly, the significant process parameters and their limits were identified using pilot experiments. Secondly, a design of experiments (3-factors with 5-levels) was conducted, according to a response surface methodology (RSM)-centre composite design (CCD), to investigate the effects of process parameters, namely, laser power, welding speed and beam offset. Thereafter, the joint strength in terms of the ultimate load was optimized to achieve a good quality weld. The responses were measured as ultimate/maximum load (UL), penetration depth (PD), weld width (WW), throat thickness (TT) and minimum distance from the root to the fusion boundary, names as *modified throat thickness* (MTT) as defined in **Fig. 1a** (schematic diagram) and **b** (actual weld). UL, WW, PD and TT have commonly been considered by many researchers [6, 34-38]. Whereas, MTT is a new response for this study. It might be presumed that the maximum probability of failure of the weld coincides with the minimum value of MTT due to the maximum stress intensity factor incurred [39]. Hence, the MTT was taken into consideration and analysed. Surrogate models for responses were developed based on experimental results and validated using the analysis-of-variance (ANOVA) technique. The 3D response surface plots were generated to establish the combined effects of input parameters on the responses. The optimised process parameters were then utilised to weld the cooling channels to module manifold. In addition to statistical evaluation of the weld joints, mechanical and metallurgical analyses were conducted on the selected samples.

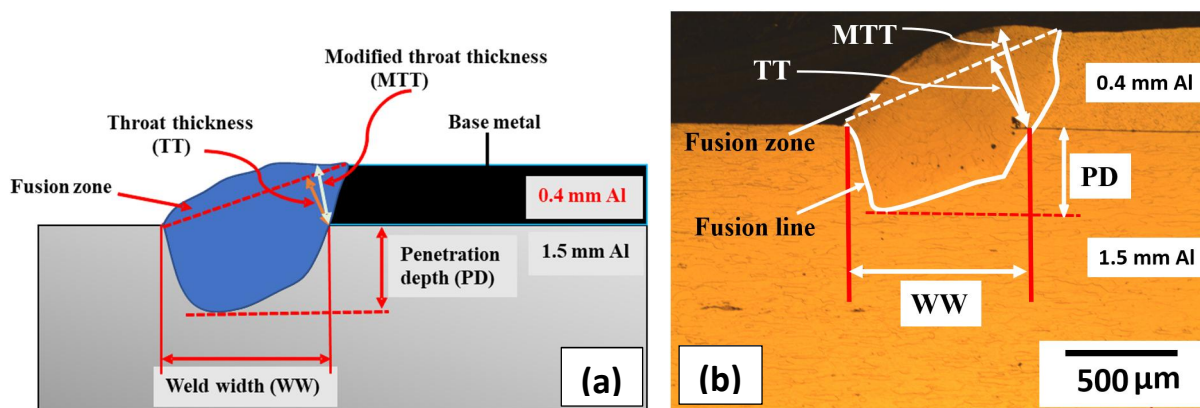


Fig. 1. Location of responses on fillet weld (a) schematic diagram and (b) actual weld

2. Experimental setup and procedure

The cooling channel and module manifold thicknesses (at the weld interface) of approximately 0.35 mm and 1.5 mm respectively as shown in **Fig. 2**. In general, cooling channels and module manifolds are made of aluminium due to their low cost, lightweight, high thermal conductivity and ease of formability/manufacturability. Therefore, the current work requires an Al/Al joint between the thin cooling channel and the relatively thick module manifold for the battery thermal management system. Before performing the laser welding of the manifold and cooling channel, trials were conducted to determine the limiting values of the welding parameters, e.g. laser power, welding speed, wobble amplitude, wobble frequency, beam incident angle and beam offset by producing fillet edge laser welds between coupons of thin Al sheets (87.5 mm × 25 mm × 0.4 mm) with a thickness representative of the walls of the cooling channel and thick Al coupons (100 mm × 25 mm × 1.5 mm) representing the module endplate (**Fig. 3a**). The base material used was AW1050A aluminium alloy having a nominal elemental composition of 0.40 wt% Fe, 0.25 wt% Si, 0.07 wt% Zn, 0.05 wt% of each Mg, Ti, Mn, Cu, 0.03 wt% other and the balance Al (i.e. ~99.5 wt%) [40]. Welding was conducted using a 1 kW YLR fibre laser (make: IPG Photonics; model: MultiAxis SYS-MA-YLR Workstation) with a constant parameter set as tabulated in **Table 2**. The welding was conducted using laser beam wobble techniques. A clamping device was used to maintain a zero gap between the two sheets. An argon gas jet emerging from a nozzle coaxial with the laser beam was used to avoid any external atmospheric contamination during welding. The limits of welding parameters used in the subsequent DoE were selected based on these experimental trials. Statistical software Minitab v19 was applied to develop the RSM design matrix.

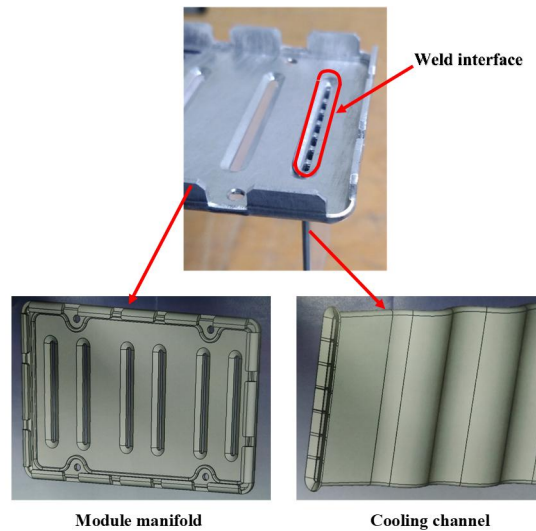


Fig. 2. The cooling channel and module manifold assembly

Table 2. Constant parameters set used in this study

| Parameter | Value/Type | Unit |
|---|------------------|---------------|
| Focus distance | 200 | mm |
| Stand-off distance | 20-23 | mm |
| Focus position | Top surface | - |
| Spot size | 28 | μm |
| Shield gas | Argon | - |
| Shield gas flow rate | 20 | l/min |
| Wobble mode | Circle Clockwise | - |
| Path diameter/radius (Wobble amplitude) | 0.5 | mm |
| Wave | CW | - |

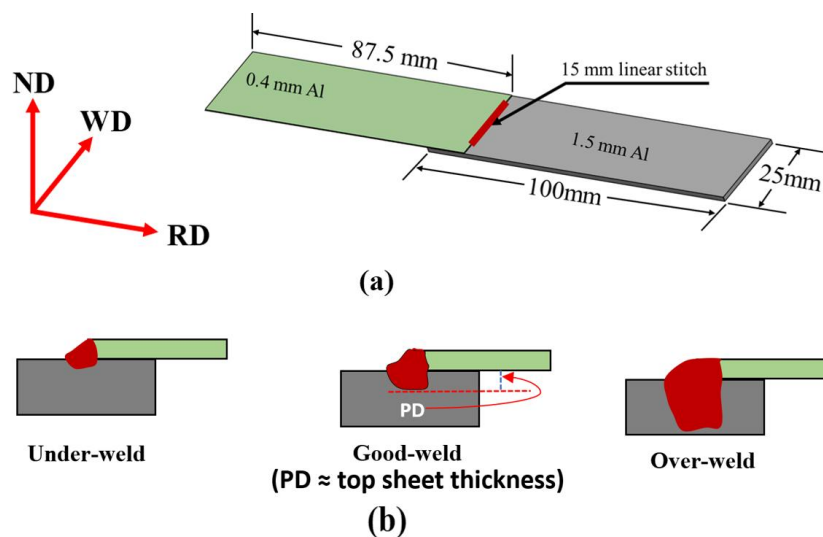


Fig. 3. Schematic diagrams of (a) joint configuration and (b) cross-sectional views from the ND (normal direction)-RD (rolling direction) sections for under weld, good weld and over weld

Measurement of the tensile strength of welded samples was conducted on an Instron 3367 test frame at a cross-head speed of 0.5 mm/min. The welded samples for metallographic analysis were sectioned perpendicular to the welding direction. In order to maintain consistency with the terminology typically used for the laser welding process, the principal directions of the laser welding geometry are referred to as RD (rolling direction), ND (normal direction) and WD (welding direction) respectively. The macrographs were acquired from the ND-RD sections of the weld seam. Based on the depth of penetration, the schematic diagram of the ND-RD sections for the under weld, good weld and over weld conditions are presented in **Fig. 3(b)**. In general, thick to thin good fillet welds, depth of penetration of the weld joint at least equal to the thickness of the thinner sheet is usually the goal. Whereas, under weld when penetration depth less than half of the top sheet thickness and the over weld when more than two times of the top sheet thickness [41]. Samples for the metallographic analysis were prepared by polishing with successively finer SiC papers, down to 1200 grade, to remove the scratches. Each sample was then polished on 3 μm , 1 μm and 0.05 μm diamond solutions. After polishing, the samples were electro-etched at 30 V using Barker's reagent (5 ml Tetrafluoroboric acid, HBF_4 + 200 ml of water) for 20 seconds [35]. The weld bead geometry in terms of WW, PD, TT and MTT was analysed using an optical microscope (Nikon Eclipse LV150N) and a micro-hardness analysis was conducted on flat metallographic specimen across the joints using a Vicker's micro-hardness testing machine (Make: Buehler's Wilson; Model: VH1202) by applying 25 gm force (i.e. 0.24 N) for 10 sec dwell time. Also, ZEISS SIGMA field emission scanning electron microscope (FE SEM) equipped with an electron backscattered diffraction (EBSD) system was used for microstructural analysis. EBSD scanning was done with 0.5 μm step size.

3. Results and discussions

This study was divided into two sections. Firstly, a pilot study was conducted to determine the effects of line energy (LE), laser beam offset and angle of incidence of the laser beam on weld quality. Secondly, optimisation was performed using desirability function analysis considering laser power, welding speed [9] and beam offset as the main welding parameters whilst wobble amplitude, wobble frequency and angle of incidence were fixed. In the research of Das et al. [9], they recommended the range of wobble amplitude and frequency to produce the successful fillet edge joint for the 0.3 mm Al to 1.5 mm Al as 0.2 – 0.7 mm and 500 – 900 Hz respectively. Hence, a few trials were performed in the aforementioned range before fixing the wobble amplitude and wobble frequency. From the trial study, it was found that the 0.5 mm wobble

amplitude was most suitable for the 0.4 mm Al to 1.5 mm Al fillet edge joint, and wobble frequency had a non-significant effect on the weld quality. Therefore, the wobble amplitude and frequency were fixed at preferred values (i.e. 0.5 mm and 600 Hz) in the present study based on the results from Das et al. [9] and pilot runs. Also, it was found that the angle of incidence had an insignificant effect on the joint quality, this will be discussed in detail in Section 3.3. In general, a major emphasis has been placed on the process parameters like laser power and welding speed by many researchers [6, 8, 9, 10, 34, 35, 38, 41, 63] but limited information is available on the effect of laser beam offset on weld quality [38]. But it could have played an important role in making a successful fillet edge weld as it ensures the edge of the upper material be melted and fused required for the leak-tight joint. Hence, it was selected as one of the input parameters to take the maximum advantage of laser beam wobbling [9]. The results of beam offset analysis may provide insights into the advantages and disadvantages of laser beam misalignment (from the joint interface) during welding.

3.1. Effect of the line energy

A few researchers have considered line energy as a key process parameter in the laser welding process [42-44]. Before parameterising the design matrix, a pilot study was performed selecting LE as a process parameter. Three parameter sets (LE1 to LE3) were chosen using different power and speed values but giving the same LE as listed in **Table 3**. Three tensile tests were performed for each parameter combination (i.e., LE1 to LE3). The average maximum load and extension with corresponding standard deviation are presented in **Table 3**.

Table 3. Process parameters for line energy study and measured responses

| Sample no. | Process parameters | | | | Results | |
|------------|--------------------|------------------------|---------------------------------------|--------------------|-----------------------------------|---------------------------------|
| | Laser power (W) | Welding speed (mm/min) | Wobble amplitude (mm)/ frequency (Hz) | Line energy (J/mm) | Average maximum load (N) \pm SD | Average extension (mm) \pm SD |
| LE1 | 400 | 4000 | 0.5/600 | 6.00 | 551.19 \pm 30.63 | 0.3278 \pm 0.015 |
| LE2 | 600 | 6000 | 0.5/600 | 6.00 | 557.31 \pm 10.81 | 0.3531 \pm 0.006 |
| LE3 | 800 | 8000 | 0.5/600 | 6.00 | 574.98 \pm 7.95 | 0.3592 \pm 0.007 |

The average maximum load and average extension for parameter combination LE1 to LE3 are plotted in **Fig. 4(a)** and **(b)** respectively. It was found that the highest maximum load and extension were achieved for the sample no. LE3 while the lowest values were obtained from the sample no. LE1.

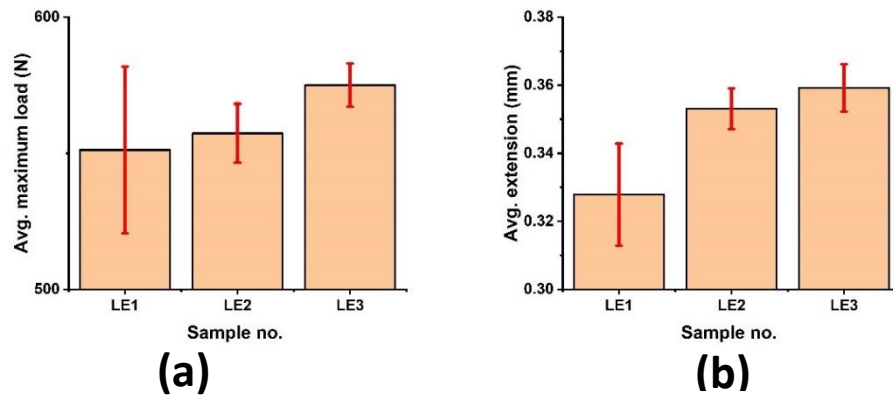


Fig. 4. Sample no. vs (a) average maximum load and (b) average extension

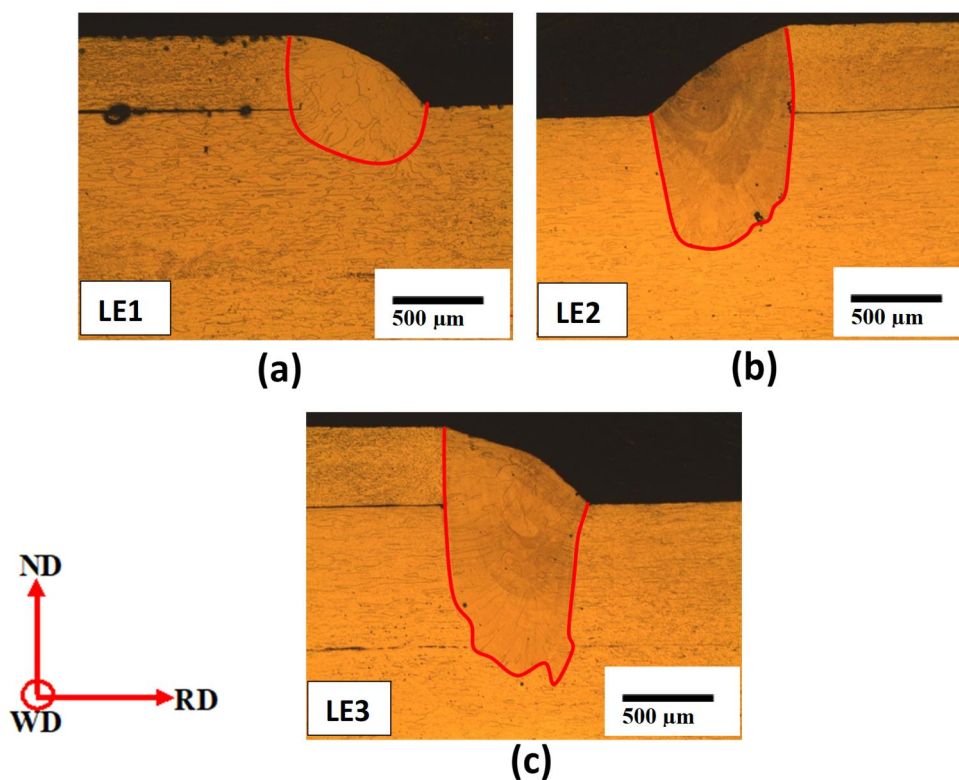


Fig. 5. Macro cross-sectional images of sample no. (a) line energy 1 (LE1), (b) line energy 2 (LE2) and (c) line energy 3 (LE3) [red lines show the fusion boundary/line]

The macro cross-sectional optical images of LE1, LE2 and LE3 are presented in **Fig. 5**. It was observed that at parametric condition LE1 (penetration depth= 261.29 μm), the joint can be categorised as under-weld (i.e. penetration depth less than half of the top sheet thickness), while an over-weld (i.e. penetration depth more than two times of the top sheet thickness) with a penetration depth of 1019.95 μm was obtained at condition LE3. A moderate depth of penetration of 659.0 μm was obtained from 600 W. Hence, the laser power should be varied around 600 W or lower with a slow welding speed to produce a good quality weld (i.e. depth

of penetration nearly equal to thinner sheet thickness). The results show that the same line energy can produce different response values and weld fusion geometry, and it is not therefore an ideal process parameter to control the fusion zone. This is due to variation in the power density, i.e. amount of power per unit volume, and the interaction time (heating time of the process on the centreline of the weld) for sample no. LE1, LE2 and LE3 [34]. Therefore, the line energy would not be considered as a process parameter for the further design of experiment study.

3.2. Effect of laser beam offset

In this section, the effect of laser beam offset was studied. The experiments were performed by varying the beam offset whilst other parameters (laser power, welding speed, wobble amplitude and frequency) remained fixed. **Fig. 6** shows the schematic diagram of laser welding at different offset positions. Sample no. B0 (**Fig. 6c**) denotes the zero-offset position of the beam, where 50% of the laser spot has been shared by both sheets. The -B2 (**Fig. 6a**) and -B1 (**Fig. 6b**) denotes the shift of beam position by 0.2 and 0.1 mm towards the 1.5 mm Al sheet respectively. Whereas, the B1 (**Fig. 6d**) and B2 (**Fig. 6e**) are the beams offset (0.1 mm and 0.2 mm) toward the 0.4 mm Al sheet over-lap region. The experimental design matrix and the measured responses are given in **Table 4**. **Fig. 7(a)** and **(b)** show sample no. vs average maximum load and extension respectively. **Fig. 8** shows the macro images of sample no. -B2, -B1, B0, B1 and B2. The results show that the highest and lowest average maximum load were obtained for samples no. B2 and -B2 respectively. This may be due to the change in the root penetration values between the joining partners/sheets. The location of root penetration of the welds (ND-RD sections) with -0.2 mm and 0.2 mm offset are shown schematically in **Fig. 9(a)** and **(b)** respectively. The root penetration can be correlated with the laser beam offset. It can be presumed that the highest and lowest root penetration values would be obtained for sample no. B2 (694.58 μm) and -B2 (396.25 μm) respectively whereas the others should remain within these upper and lower values. The deviation of laser beam to 1.5 mm Al side from 0.2 mm offset (-B2) produced either lack of fusion at the root and lack of penetration at the face of the weld (**Fig. 8a**). Due to the small width of the fusion zone, and the improvement of maximum load is attributed to higher root/bond width [38]. As shown in **Fig. 8a** and **8e**, deviation of beam location from -B2 to B2 leads to an increase in root/bond width by about 76%. Also, the throat thickness for sample no. B2 (377.46 μm) was higher than sample no. -B2 (204.26 μm). Subsequently, the maximum joint load was achieved for sample no. B2 and minimum for -B2. In addition, a consistent trend was obtained for the average maximum load vs root penetration

where an increasing value of maximum load was obtained from sample no. -B2 to B2 due to an increase in root penetration value. Also, it was observed that the sample having a comparatively high maximum load (e.g. B0) had a lower extension value than the sample with a lower maximum load (e.g. -B1) and vice-versa. The highest average maximum extension was obtained for sample no. B1 which was 0.42% higher than sample no. B2 and the corresponding maximum loads obtained were 612.08 N and 623.23 N respectively. Thus, beam offset had a non-significant effect on extension.

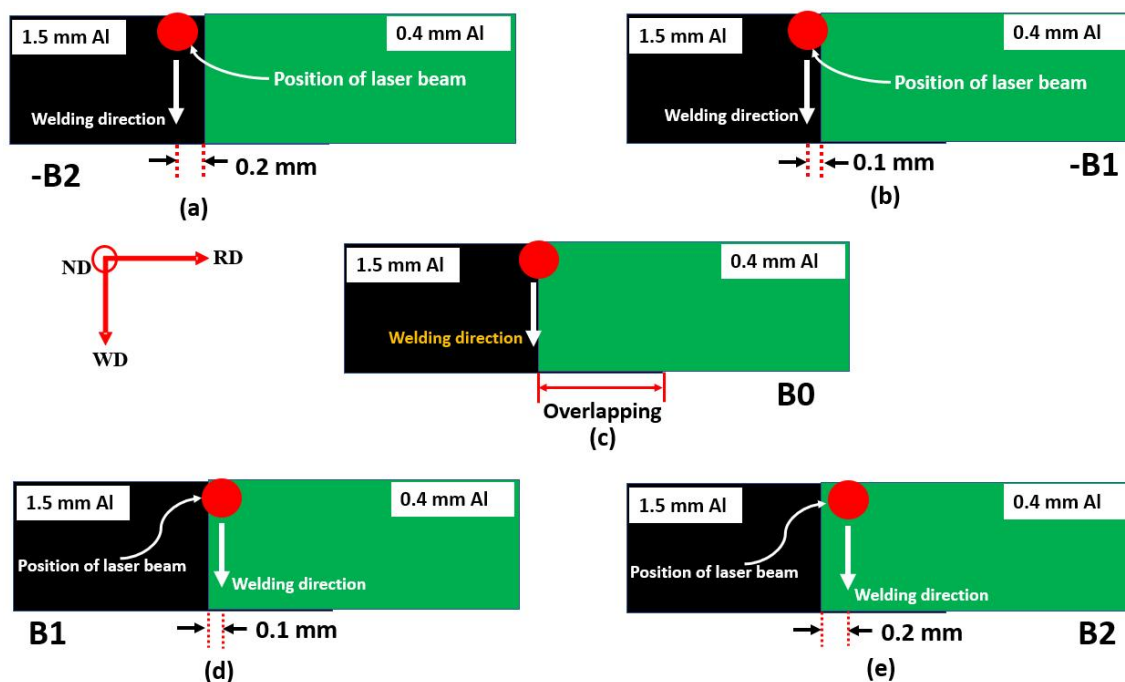


Fig. 6. Schematic diagram of laser welding at different offset position (a) -0.2 mm offset (-B2), (b) -0.1 mm offset (-B1), (c) 0 offset (B0), (d) 0.1 mm offset (B1) and (e) 0.2 mm offset (B2)

Table 4. Process parameters for laser beam offset study and measured responses

| Sample no. | Process parameters | | | | Responses | |
|------------|--------------------|------------------------|---------------------------------------|-------------|-----------------------------------|---------------------------------|
| | Laser power (W) | Welding speed (mm/min) | Wobble amplitude (mm)/ frequency (Hz) | Offset (mm) | Average maximum load (N) \pm SD | Average extension (mm) \pm SD |
| -B2 | 400 | 4000 | 0.5/600 | 0.2 | 258.59 \pm 26.47 | 0.1999 \pm 0.033 |
| -B1 | 400 | 4000 | 0.5/600 | 0.1 | 512.57 \pm 26.10 | 0.3426 \pm 0.020 |
| B0 | 400 | 4000 | 0.5/600 | 0.0 | 551.19 \pm 30.63 | 0.3278 \pm 0.015 |
| B1 | 400 | 4000 | 0.5/600 | 0.1 | 612.08 \pm 8.73 | 0.4025 \pm 0.020 |
| B2 | 400 | 4000 | 0.5/600 | 0.2 | 623.23 \pm 10.38 | 0.4008 \pm 0.025 |

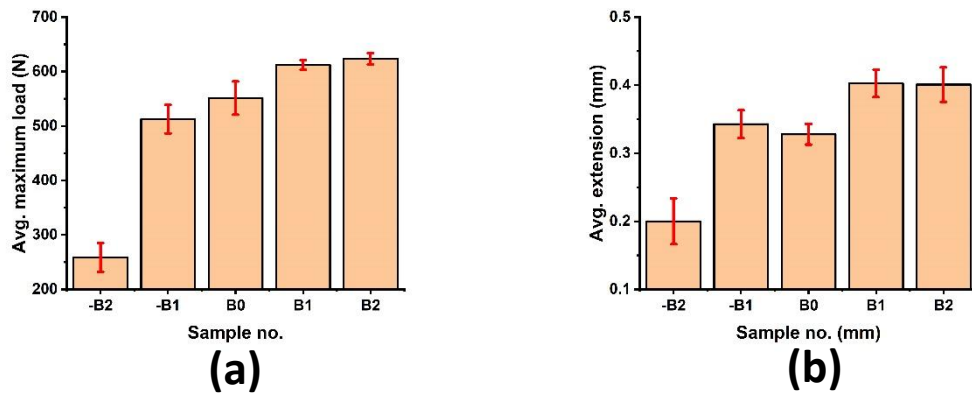


Fig. 7. Sample no. vs (a) average maximum load and (b) average extension

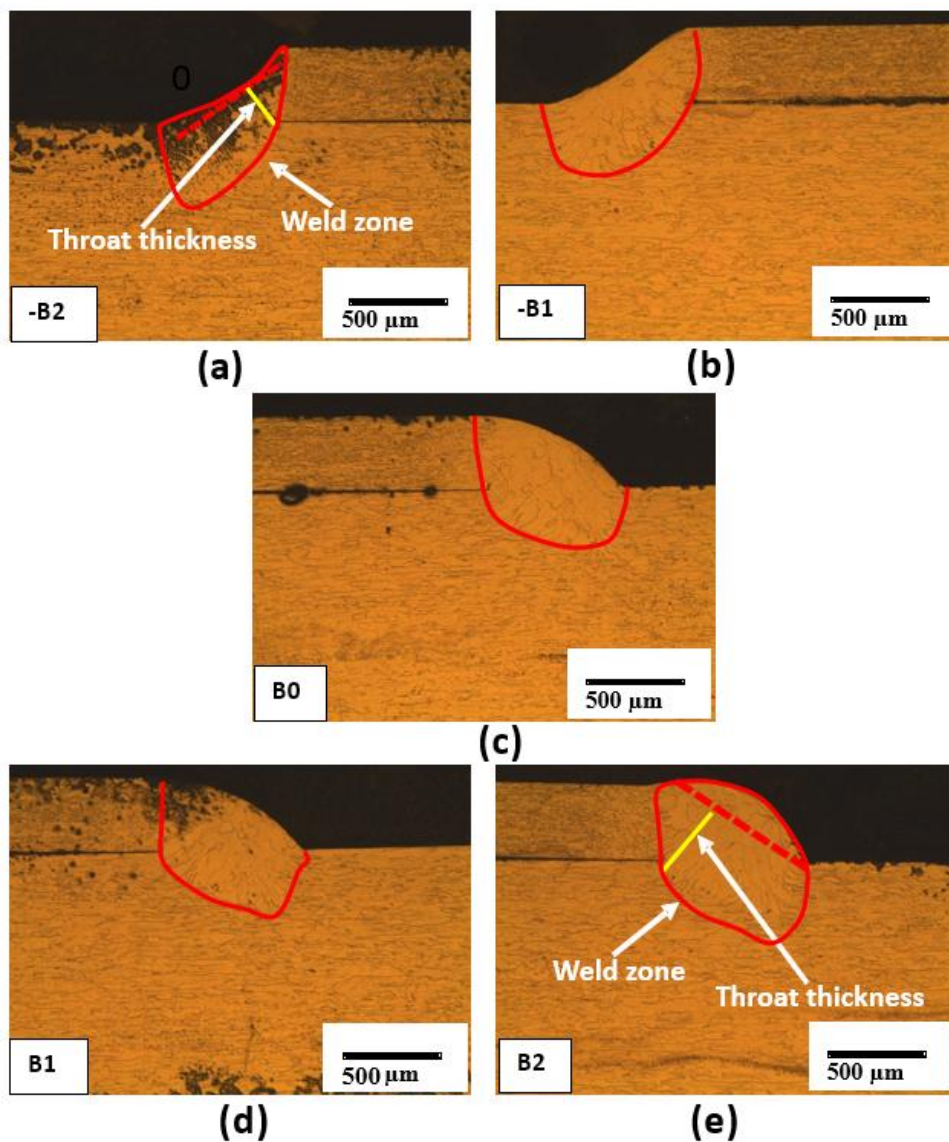


Fig. 8. Macro image of sample no. (a) -0.2 mm offset (-B2), (b) -0.1 mm offset (-B1), (c) 0 offset (B0), (d) 0.1 mm offset (B1) and (e) 0.2 mm offset (B2)

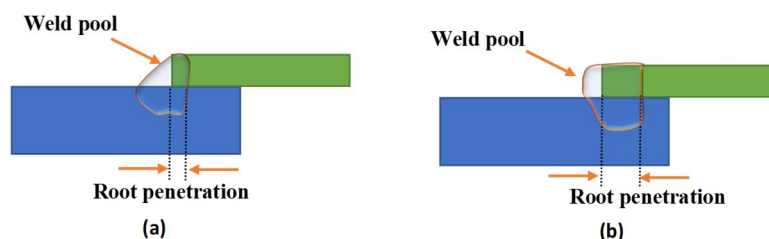


Fig. 9. Schematic diagram of the effective sharing area between the plates for (a) -0.2 mm offset and (b) 0.2 mm offset

3.3. Effect of beam incident angle

The laser beam incident angle might be considered as one of the significant process parameters [6, 37]. Experimental trials were completed with different angles of incidence (0° , 10° and 15°) whilst the laser power and welding speed were kept constant. A schematic diagram of laser welding with the angle of incidence is shown in **Fig. 10**. The process parameters and measured values of the responses are presented in **Table 5**. **Fig. 11(a)** and **(b)** show the angle of incidence vs average maximum load and average extension plot respectively. The highest maximum load occurred with an angle of incidence of 15° with a value of 573.38 N which was 2.8% higher than the 0° weld sample. From the results, it can be concluded that the effect of the angle of incidence is not significant on the maximum load and extension which can be sustained by the welded joint and was considered for further experimentation.

Table 5. Process parameters incident angle study and measured responses

| Sample no. | Process parameters | | | | Responses | |
|------------|---------------------------------|------------------------|---------------------------------------|-----------------|---------------------------------------|---------------------------------|
| | Angle of incidence ($^\circ$) | Welding speed (mm/min) | Wobble amplitude (mm)/ frequency (Hz) | Laser power (W) | Average maximum load (N) \pm SD (N) | Average extension (mm) \pm SD |
| A0 | 0 | 6000 | 0.5/600 | 600 | 557.31 \pm 10.81 | 0.3531 \pm 0.006 |
| A10 | 10 | 6000 | 0.5/600 | 600 | 565.96 \pm 1.04 | 0.4036 \pm 0.016 |
| A15 | 15 | 6000 | 0.5/600 | 600 | 573.38 \pm 7.63 | 0.3923 \pm 0.020 |

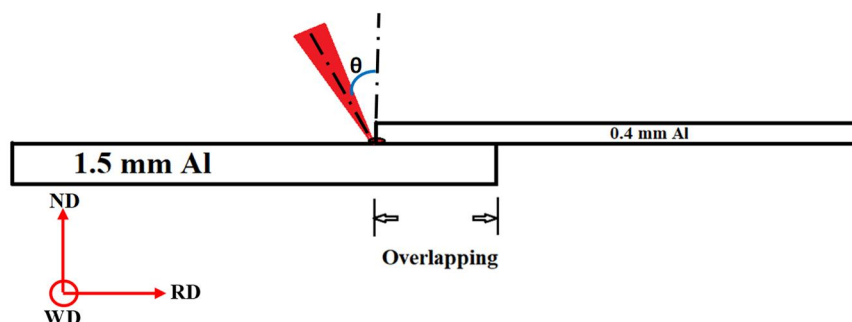


Fig. 10. Schematic diagram of laser welding at beam incidence

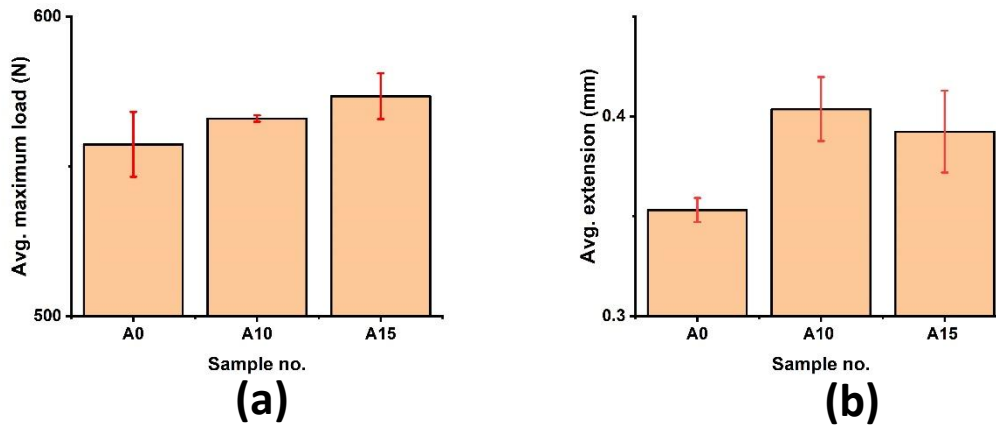


Fig. 11. Effect of angle of incidence on (a) average maximum load and (b) average extension

3.4. Main experimentation using RSM-CCD matrix

This section describes in detail the optimization of laser welding process parameters (laser power, welding speed and beam offset) through the mechanical, microstructural and statistical approach. The selection of process parameters was done based on the foregoing pilot studies and their significance. The process parameters such as laser power and welding speed are more commonly considered in the literature for laser welding but in addition, beam offset was selected in this study as one of the important parameters to correlate with responses. The welded joints were prepared under varying levels of input parameters (**Table 6**). As described section 3.2 the negative offset values denote the shift of beam towards the 1.5 mm Al sheets while positive offset values denote shift towards the 0.4 mm Al sheets. Zero offsets denote the 50% sharing of the laser beam by two sheets. The design of experiment was made considering central composite response surface design (in which a second-order model can be developed efficiently) including six centre points using Minitab v19 software. Each experiment was performed three times and the average values of responses are reported in **Table 7**. The average maximum load of the samples is denoted by the ultimate load (UL) in Table no. 7. Weld quality was assessed on the ultimate load (i.e.; average maximum load achieved by the welded samples/component in load vs extension plot). Finally, desirability function analysis was applied for the optimization of UL.

Table 6. Process parameters and their limits

| Parameters with units | Notation | Levels | | | | |
|-----------------------|----------|--------|-------|------|------|---------|
| | | -2 | -1 | 0 | +1 | +2 |
| Power, W | P | 331.80 | 400 | 500 | 600 | 668.10 |
| Welding speed, mm/min | S | 659.10 | 1000 | 1500 | 2000 | 2340.90 |
| Beam offset, mm | OFF | -0.20 | -0.12 | 0 | 0.12 | 0.20 |

Table 7. CCD matrix for actual factors and measured experimental results

| Exp. no. | Process parameters | | | Responses | | | | |
|----------|--------------------|-----------|---------|--------------------|-----------------------|-----------------------|-----------------------|------------------------|
| | P(W) | S(mm/min) | OFF(mm) | UL(N) \pm SD | PD(μ m) \pm SD | WW(μ m) \pm SD | TT(μ m) \pm SD | MTT(μ m) \pm SD |
| 1 | 600.0 | 2000.0 | 0.12 | 577.91 \pm 20.40 | 880.855 \pm 10.23 | 1070.064 \pm 11.45 | 397.895 \pm 6.25 | 400.641 \pm 4.15 |
| 2 | 500.0 | 1500.0 | 0.00 | 537.17 \pm 4.77 | 762.764 \pm 3.55 | 901.274 \pm 2.36 | 367.024 \pm 1.55 | 376.384 \pm 1.36 |
| 3 | 500.0 | 2340.9 | 0.00 | 557.40 \pm 27.03 | 599.999 \pm 18.30 | 863.057 \pm 25.08 | 389.018 \pm 9.3 | 371.159 \pm 8.25 |
| 4 | 500.0 | 1500.0 | 0.00 | 527.84 \pm 13.43 | 689.368 \pm 14.83 | 926.752 \pm 11.43 | 383.2 \pm 7.93 | 374.726 \pm 8.36 |
| 5 | 600.0 | 2000.0 | -0.12 | 510.49 \pm 3.55 | 829.791 \pm 1.15 | 936.306 \pm 2.55 | 350.805 \pm 1.05 | 347.635 \pm 0.58 |
| 6 | 400.0 | 1000.0 | 0.12 | 584.84 \pm 15.92 | 408.51 \pm 11.88 | 831.21 \pm 19.92 | 375.564 \pm 5.88 | 392.337 \pm 5.29 |
| 7 | 500.0 | 1500.0 | 0.00 | 534.16 \pm 27.80 | 609.581 \pm 24.80 | 920.382 \pm 21.77 | 368.024 \pm 12.7 | 389.407 \pm 10.28 |
| 8 | 331.8 | 1500.0 | 0.00 | 563.72 \pm 7.80 | 213.853 \pm 6.99 | 694.268 \pm 8.51 | 358.389 \pm 3.99 | 387.94 \pm 6.37 |
| 9 | 600.0 | 1000.0 | -0.12 | 523.09 \pm 22.82 | 987.288 \pm 19.07 | 1194.268 \pm 20.22 | 374.34 \pm 9.09 | 365.491 \pm 7.25 |
| 10 | 668.1 | 1500.0 | 0.00 | 536.40 \pm 4.50 | 1025.424 \pm 6.57 | 1232.484 \pm 5.50 | 375.728 \pm 3.57 | 382.532 \pm 2.15 |
| 11 | 400.0 | 2000.0 | -0.12 | 390.46 \pm 29.45 | 444.915 \pm 33.41 | 605.096 \pm 27.27 | 316.643 \pm 13.41 | 299.885 \pm 12.47 |
| 12 | 500.0 | 659.10 | 0.00 | 528.41 \pm 6.07 | 838.983 \pm 6.25 | 1101.911 \pm 6.96 | 369.091 \pm 4.29 | 380.558 \pm 2.36 |
| 13 | 500.0 | 1500.0 | 0.00 | 527.68 \pm 8.60 | 707.627 \pm 5.85 | 949.045 \pm 7.60 | 364.892 \pm 2.65 | 366.906 \pm 1.28 |
| 14 | 500.0 | 1500.0 | 0.00 | 539.77 \pm 2.22 | 694.915 \pm 0.85 | 990.446 \pm 0.57 | 370.355 \pm 0.82 | 381.181 \pm 0.27 |
| 15 | 500.0 | 1500.0 | -0.20 | 438.99 \pm 24.05 | 711.864 \pm 21.26 | 1047.771 \pm 23.05 | 296.21 \pm 10.26 | 300.037 \pm 7.29 |
| 16 | 400.0 | 1000.0 | -0.12 | 445.45 \pm 8.46 | 559.322 \pm 9.47 | 856.688 \pm 10.76 | 305.094 \pm 8.37 | 323.667 \pm 6.32 |
| 17 | 400.0 | 2000.0 | 0.12 | 562.79 \pm 6.93 | 375.527 \pm 8.23 | 798.301 \pm 7.93 | 360.985 \pm 4.23 | 415.889 \pm 5.31 |
| 18 | 500.0 | 1500.0 | 0.00 | 534.30 \pm 8.46 | 713.08 \pm 8.52 | 963.907 \pm 9.51 | 360.58 \pm 3.52 | 376.749 \pm 2.04 |
| 19 | 600.0 | 1000.0 | 0.12 | 550.76 \pm 5.38 | 957.806 \pm 6.02 | 1280.255 \pm 4.28 | 407.957 \pm 4.32 | 410.569 \pm 6.01 |
| 20 | 500.0 | 1500.0 | 0.20 | 559.15 \pm 4.17 | 616.034 \pm 8.12 | 963.907 \pm 4.22 | 397.028 \pm 5.12 | 429.487 \pm 4.82 |

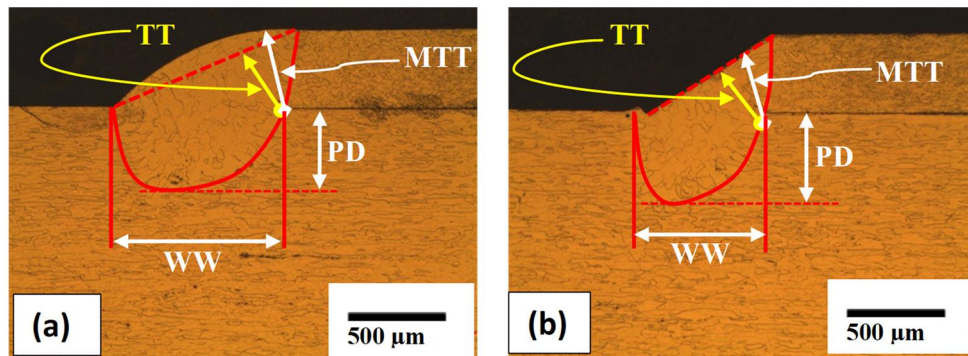


Fig. 12. Macro view of the sample with (a) maximum ultimate load (sample no. 6) and (b) minimum ultimate load (sample no. 11)

It should be observed that none of the experiments fully penetrated the bottom sheet (1500 μ m Al) which was consistent with the requirements for a good weld. The maximum PD was 1025.424 μ m which was 31.6% less than the bottom sheet thickness (1500 μ m). The maximum and minimum values of the ultimate load or average maximum load was obtained for experiments no. 6 and 11 respectively and their macro images are presented in **Fig. 12**. The fitted quadratic polynomial model for responses was statistically significant for the prediction within the range of process parameters and therefore used for further analysis.

3.4.1. EBSD analysis of weld metals

Fig. 13 shows the inverse pole figure (IPF) maps obtained from the ND-RD section of the BM and weld metals. The EBSD micrographs of upper and lower as-received Al base materials (BM) are shown in **Fig. 13a** and **Fig. 13b** respectively. Also, the micrographs of the welded samples, sample no. 6 and sample no. 11 (**Table 7**) are presented in **Fig. 13c** and **Fig. 13d**

respectively. These joints were also under the category of a good and bad weld. IPF maps of weld metals (**Fig. 13c** and **Fig. 13d**) highlighted three distinguishable regions marked as fusion zone 1 (FZ1), fusion zone 2 (FZ2) and fusion zone 3 (FZ3) extended from fusion boundary (FB) to the weld centre. These are characterised by straight and broad columnar grains in FZ1 and fine equiaxed grains in FZ2 and FZ3 and are due to the change in solidification mode i.e., change in the ratio of temperature gradient and growth rate (G/R ratio). The mode of solidification can be planar, cellular, columnar dendritic, and equiaxed dendritic depending on the solidification condition and the material system involved [45]. The typical columnar grain structure in FZ1 was obtained due to the dendritic growth from the fusion line during solidification. However, grain growth direction on both the samples (i.e. sample no. 6 and 11) was identical from straight and broad columnar grains (FZ1) to fine equiaxed grains (FZ2) than coarse equiaxed grains (FZ3). The grain size of the different fusion zones such as FZ1, FZ2 and FZ3 for sample no. 6 was around 65, 45 and 90 μm respectively. Whereas, for sample no. 11, the grain size was around 55, 40 and 80 μm for FZ1, FZ2, and FZ3 respectively. A linear intercept method was used for the measurement of the grain size. Although, the laser power was equal for both sample no. 6 and sample no. 11. But the welding speed of sample no. 6 was half of the sample no. 11. Due to large grain sizes for sample no. 6, and the coarsening of grain size is attributed to the slow cooling rate [6, 63]. However, as given in **Table 7**, deviation of beam location from 0.12 mm to -0.12 mm for sample no. 6 and sample no. 11 respectively owing to an increase in bond width by about 38%. Consequently, the high joint load was achieved for sample no. 6 and low for sample no. 11 [38].

Grain boundary fraction of high (HAGB) and low angle (LAGB) grain boundaries in both the weld categories (i.e. sample no. 6 and sample no. 11) were calculated from the EBSD map (**Fig. 13**). HAGBs create obstacles for gliding dislocations which increases the dislocation density at the vicinity of the grain boundary. The piled-up dislocations create a back stress which resists dislocation movement under the stress/strain field. The plasticity proceeds only when higher strain energy has been achieved [46, 47]. **Fig. 14** shows the degree of misorientation occurred in the weld metals. Sample no. 6 shows a higher high angle grain boundary (HAGB) fraction followed by sample no. 11. Similarly, the opposite trend has been observed in the case of low angle grain boundary (LAGB) fractions of weld metals. Therefore, sample no. 6 having a higher HAGB fraction should provide a comparatively higher tensile load [23] than the other weld metal (sample no. 11) because the dislocation pile-ups along the HAGB should act as a precursor to solid-state phase transformation under true plastic

deformation and the rate of transformation should depend upon the relative concentration of pile-ups. Again, higher grain boundary energy which incorporates heterogeneous nucleation of dislocations within the grains under stress field. This heterogeneous nucleation of dislocations increases the dislocation density within the grain and helps to increase the tensile strength. Therefore, the results obtained from the EBSD is well aligned with the experimental trials, i.e. sample no. 6 gave the higher UL than sample no. 11.

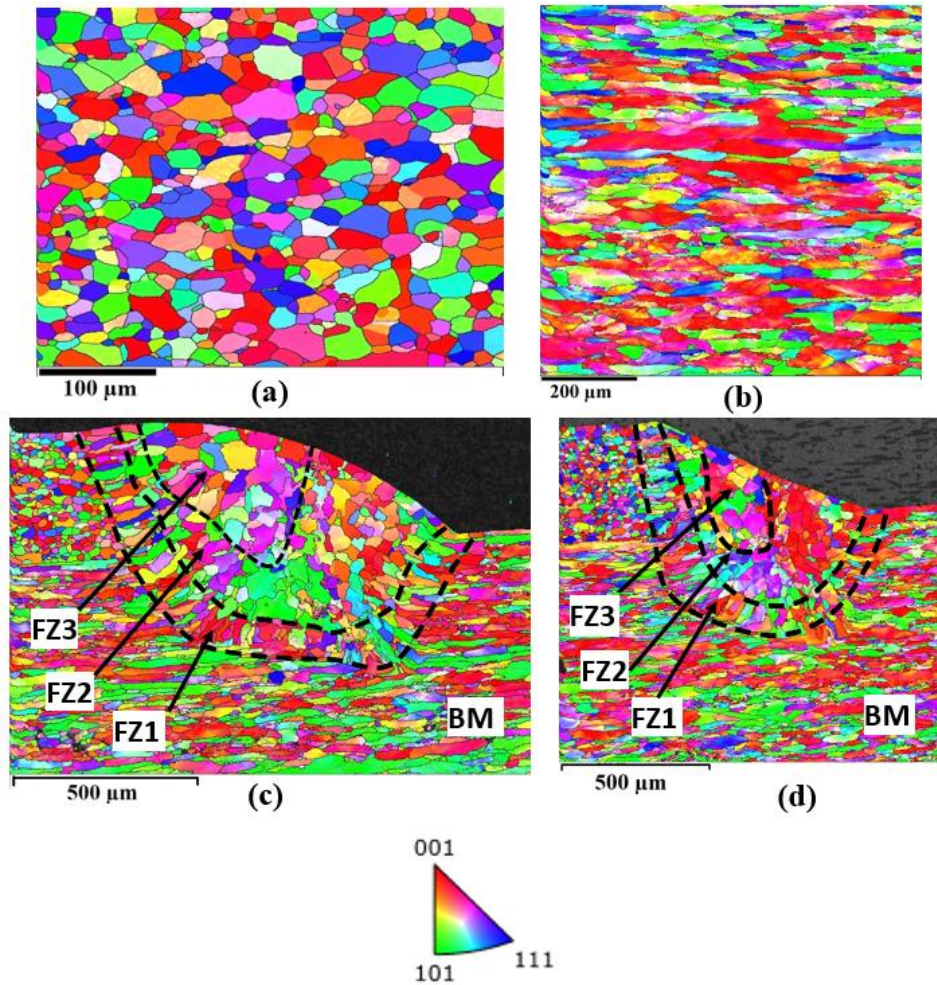


Fig. 13. IPF maps of (a) upper BM, (b) lower BM, (c) sample no. 6 and (d) sample no. 11

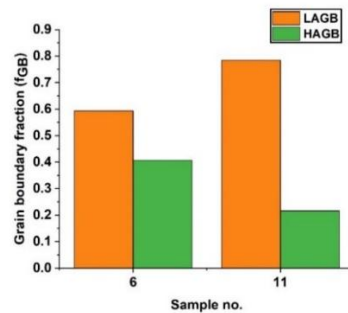


Fig. 14. Distribution of low angle and high angle grain boundaries in different laser welded samples

3.4.2. Micro-hardness analysis

In order to evaluate the micro-hardness profile of the fillet edge joint, the test was conducted for the maximum and minimum ultimate load samples (sample no. 6 and 11). A total of 20 indents were distributed in the upper sheet, fusion zone and lower sheet as shown in **Fig. 15**. From **Fig. 15**, the micro-hardness profile was measured by entering the fusion zones (FZs) from the upper base metal and leaving the fusion zone to the lower base metal. Micro-hardness was repeated three times on separate sections to guarantee reliable data and to evaluate the standard deviation. A similar hardness profile was observed for both samples no. 6 and 11 as shown in **Fig. 15a** and **b** respectively. The hardness value of the upper base metal was recorded in the range of 38.1–39.1 HV_{0.025} with an average hardness of 38.6 HV_{0.025}.

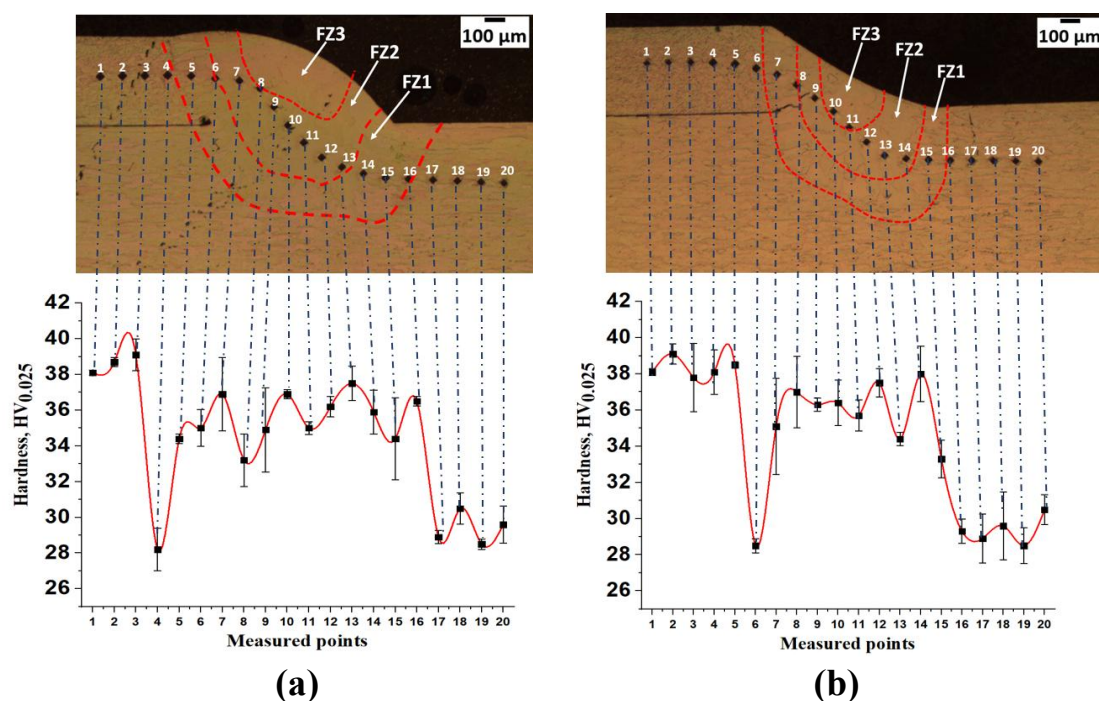


Fig. 15. Microhardness profiles of (a) sample no. 6 and (b) sample no. 11

Whereas, the hardness values for the lower base metal was measured in the range of 28.5–30.5 HV_{0.025} with an average hardness of 29.5 HV_{0.025}. Micro-hardness of the fusion zones (FZs) varies from 33.2–38 HV_{0.025} with an average hardness of 35.6 HV_{0.025}. It can be seen that the micro-hardness increased slightly (by up to 21%) in the FZs in comparison with the lower parent metal and, decreased slightly (by up to 8%) in comparison to the upper base metal. The maximum micro-hardness was measured as 37.5 HV_{0.025} and 38 HV_{0.025} for sample no. 6 and 11 respectively when the micro-hardness is measured in FZ2. As shown in **Fig. 13c** and **d**, EBSD maps the smallest grains are obtained at the FZ2 area which is attributed to high micro-

hardness values. A non-consistent trend was observed in the FZs of both the weld metals. This is due to the fact that the FZs were formed from the mixture of the two different as-received base metals structure as shown in **Fig. 13a** and **b**, no filler materials were added, and it was difficult to achieve a homogeneous microstructure, consequently, the irregular distributions of the precipitates (especially Mg precipitates [48]). It is evident from the EBSD maps (**Fig. 13c** and **d**) that the fusion/melt regions (i.e., FZ1, FZ2 and FZ3) of both samples no. 6 and 11 almost equally solidify in all orientation such as 001, 101 and 111 when the weld area is observed in ND-RD plane. Therefore, the localized hardness variation may be attributed to fusion zone grain orientation. Also, a few studies were reported where grain orientation had a significant effect on localized hardness [64, 65], and Das et al. [41] were achieved a similar trend of micro-hardness profile for the laser-welded AA 5182.

In general, the micro-hardness of a welded joint depends on the metallurgical condition of the weld material and the possible presence of defects [49]. Though, an ideal weld has the same metallurgy and shape as the original base material without defects. But the reality of aluminium welding was usually that the metallurgical properties deteriorated, the shape might be better or worse than base material and defects will always appear [50, 51].

3.4.3. Development of surrogate models

The adequacy of the developed models and the test for significance on individual model coefficients were performed using the sequential analysis-of-variance (ANOVA) technique using the Minitab v19 software to obtain the best-fit models. The purpose of ANOVA is to investigate which process parameter/s significantly affect each quality characteristic. **Table 8** shows the analysis-of-variance of the responses (UL, PD, WW, TT and MTT) and presents the F-value, p-value and percentage of contribution (POC) of the significant model ($p < 0.05$) at 95% confidence level. The F-value in the ANOVA test also determines the p-value, a p-value less than 0.05 (typically ≤ 0.05) is statistically significant and, a p-value higher than 0.05 (> 0.05) is not statistically significant [6, 52]. The significant factors are highlighted in **Table 8**. Quadratic models were found to best fit the data when compared to linear, 2FI and cubic models based on a highly significant p-value. The $F_{\text{statistics}}$, p-value and POC were used in the analysis to test the significant factors. The ANOVA table also shows the other adequacy measure, i.e. R^2 for the response and, the adequacy measures were greater than 85%, which are reasonable and indicate the models are effective. The results from ANOVA for the UL, the offset (OFF), the interaction effect of laser power and offset ($P * \text{OFF}$) and the quadratic effect of the offset (OFF^2) were the significant model terms. Secondly for the PD, the laser power (P), welding

speed (S), beam offset (OFF) and the quadratic effect of power (P^2) were the significant model terms. Laser power (P) and welding speed (S) were the significant terms for the WW. For TT, the P, OFF and OFF^2 were the significant terms. Finally, OFF and the interaction effect of laser power and offset ($P * OFF$) were the significant model terms for MTT. The other model terms were not significant. It can be concluded from the POC of the ANOVA table; the beam offset had commonly shown a most significant effect on UL, TT and MTT with POC of 60.3, 60.3 and 82.7 respectively which signified the importance of laser beam offset for producing the high strength fillet edge weld. Whereas, the laser power had the most significant effect on PD and WW with POC of 89.1 and 71.6 respectively. Also, in the research of Das et al. [9], the laser power was found as the most significant factor for controlling the penetration depth and weld width efficiently for Al-Al fillet edge joints.

Table 8. ANOVA for the fitted quadratic model for responses

| ANOVA terms | Responses | | | | | | | | | | | | | | |
|-------------|-----------|---------|------|---------|---------|------|---------|---------|------|---------|---------|------|---------|---------|------|
| | UL | | | PD | | | WW | | | TT | | | MTT | | |
| Source | F-value | p-value | POC | F-value | p-value | POC | F-value | p-value | POC | F-value | p-value | POC | F-value | p-value | POC |
| Model | 8.21 | 0.00 | | 61.92 | 0.00 | | 16.39 | 0.00 | | 8.45 | 0.00 | | 19.71 | 0.00 | |
| P | 2.44 | 0.15 | 2.90 | 505.87 | 0.00 | 89.1 | 112.76 | 0.00 | 71.6 | 15.88 | 0.00 | 18.4 | 4.31 | 0.06 | 2.30 |
| S | 0.03 | 0.87 | 0.03 | 29.74 | 0.00 | 5.24 | 28.53 | 0.00 | 18.1 | 0.00 | 0.95 | 0.00 | 1.19 | 0.30 | 0.63 |
| OFF | 50.67 | 0.00 | 60.3 | 6.27 | 0.03 | 1.10 | 1.30 | 0.28 | 0.82 | 51.94 | 0.00 | 60.3 | 155.13 | 0.00 | 82.7 |
| P*S | 1.93 | 0.19 | 2.30 | 0.63 | 0.44 | 0.11 | 1.23 | 0.29 | 0.78 | 0.62 | 0.44 | 0.72 | 0.80 | 0.39 | 0.42 |
| P*OFF | 25.05 | 0.00 | 21.7 | 4.83 | 0.05 | 0.85 | 0.10 | 0.76 | 0.06 | 0.77 | 0.40 | 0.89 | 7.93 | 0.01 | 4.23 |
| S*OFF | 1.26 | 0.28 | 1.49 | 2.17 | 0.17 | 0.38 | 2.60 | 0.13 | 1.64 | 0.11 | 0.75 | 0.13 | 3.23 | 0.10 | 1.72 |
| P^2 | 0.29 | 0.60 | 0.34 | 5.49 | 0.04 | 0.96 | 0.00 | 0.95 | 0.00 | 0.13 | 0.73 | 0.14 | 0.28 | 0.60 | 0.15 |
| S^2 | 0.02 | 0.90 | 0.01 | 1.22 | 0.29 | 0.21 | 0.15 | 0.71 | 0.09 | 0.67 | 0.43 | 0.78 | 0.39 | 0.54 | 0.20 |
| OFF^2 | 5.86 | 0.03 | 6.98 | 0.66 | 0.43 | 0.11 | 0.84 | 0.38 | 0.53 | 5.55 | 0.04 | 6.45 | 3.98 | 0.07 | 2.12 |
| R^2 | 88.08% | | | 98.24% | | | 93.65% | | | 88.38% | | | 94.66% | | |

The surrogate models for responses (Eqs. i - v), which can be used for prediction within the same design space, in terms of actual factors were shown below:

$$UL (N) = 748 - 0.572 * P - 0.125 * S + 1274 * OFF + 0.000227 * P * S - 2.263 * P * OFF + 0.153 * S * OFF + 0.000328 * P^2 + 0.000003 * S^2 - 1024 * OFF^2 \quad (i)$$

$$PD (\mu m) = -977 + 5.09 * P - 0.141 * S - 1985 * OFF - 0.000218 * P * S + 2.52 * P * OFF + 0337 * S * OFF - 0.00240 * P^2 + 0.000045 * S^2 - 579 * OFF^2 \quad (ii)$$

$$\begin{aligned}
 WW (\mu\text{m}) = & 44 + 2.45 * P - 0.010 * S - 953 * OFF - 0.000459 * P * S + 0.54 * P * OFF + 0.555 * S \\
 & * OFF - 0.00009 * P^2 + 0.000024 * S^2 + 983 \\
 & * OFF^2
 \end{aligned}
 \tag{iii}$$

$$\begin{aligned}
 TT (\mu\text{m}) = & 233 + 0.390 * P + 0.0022 * S + 440 * OFF - 0.000076 * P * S - 0.355 * P * OFF - 0.0264 \\
 & * S * OFF - 0.000128 * P^2 + 0.000012 * S^2 - 591 \\
 & * OFF^2
 \end{aligned}
 \tag{iv}$$

$$\begin{aligned}
 MTT (\mu\text{m}) = & 372.2 + 0.012 * P + 0.0495 * S + 584 * OFF - 0.000069 * P * S - 0.902 * P * OFF \\
 & + 0.1151 * S * OFF + 0.000153 * P^2 - 0.000007 * S^2 - 397 \\
 & * OFF^2
 \end{aligned}
 \tag{v}$$

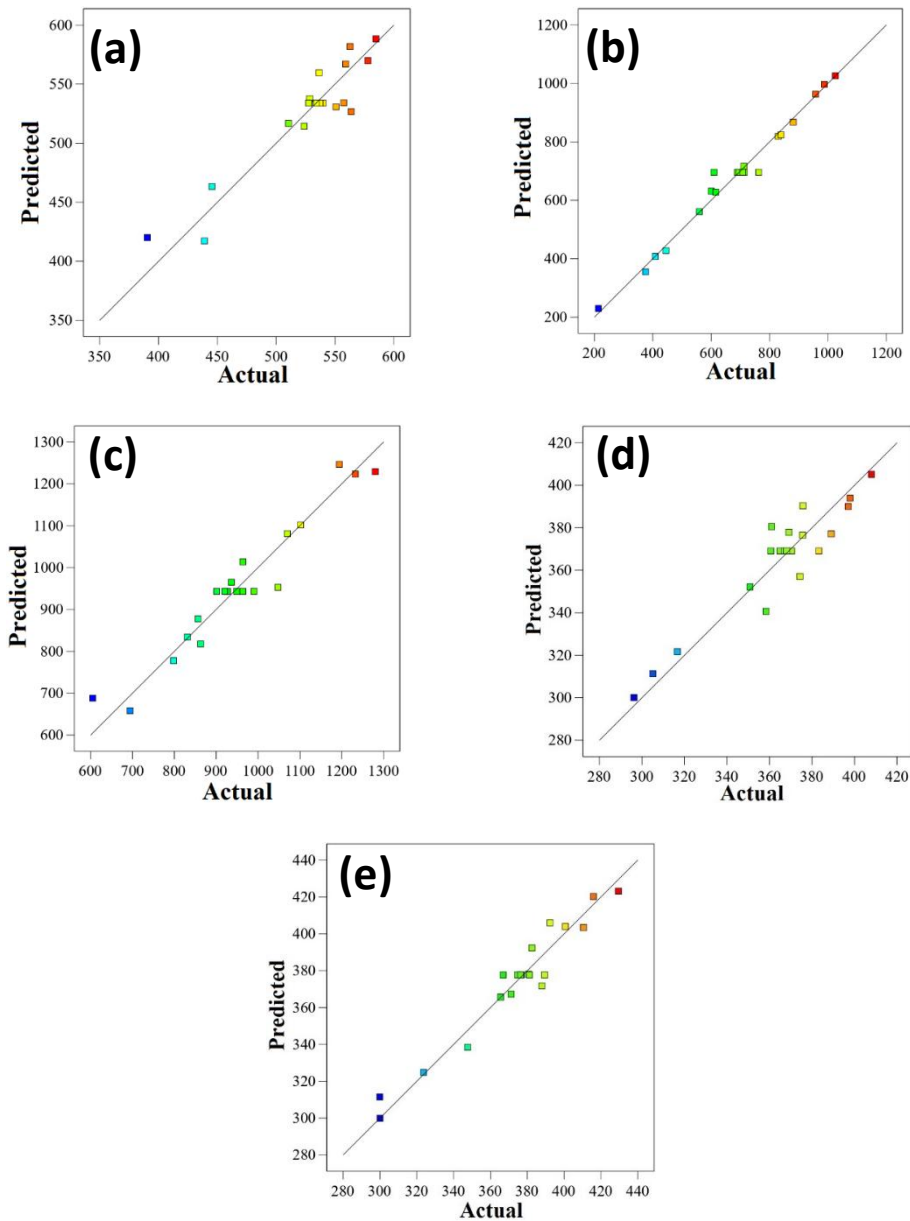


Fig. 16. Actual vs predicted plot for (a) ultimate load (UL), (b) penetration depth (PD), (c) weld width (WW), (d) throat thickness (TT) and (e) modified throat thickness (MTT)

Fig. 16a-e present the relationship between the actual and predicted values (from the surrogate models) of the UL, PD, WW, TT and MTT respectively. The figures indicate that the developed surrogate models (**Eqs. i – v**) were adequate and predicted results are in good agreement with measured data. The model can be used to navigate/prediction within the same design space.

3.4.4. Effect of the input parameters on responses

The 3D response surface and contour plots for the effect of process parameters on responses have been constructed according to the fitted quadratic models (**Eqs. i - v**). **Fig. 17 - 21** shows the surface plots for responses (UL, PD, WW, TT and MTT) with one variable kept constant at their respective centre value and the other two within the working range.

In terms of an interaction between the power and offset, as shown in **Fig. 17(a)**, the UL is maximum at lower values of laser power and maximum values of offset. This might be due to the lower power promoting the faster cooling [53] (small and more equiaxed grain) and higher offset providing more sharing/weld area between the sheets. It is evident from **Fig. 17(b)** that UL increases with increasing welding speed at high power, whilst decreasing at lower laser power. This is because, at low power and high welding speed, lower power density is generated, resulting in a lack of penetration and thus, a weak joint. Further, with a high value of laser power and welding speed towards the maximum value, the UL is improved as interaction time decreases and power density increases and maximum strength is obtained. While at a high value of laser power and slower welding speed, the depth focus is larger due to the higher rate of increase of specific point energy with longer interaction times causing decomposition of material (overheating) and resulting in low joint strength [54].

From **Fig. 17(c)**, it can be seen that increasing the offset from -0.2 mm to +0.2 mm, increases UL. At the lower level value of offset (-0.2 mm), the reduced shared area between the sheets results in low joint strength. At the higher level of offset (+0.2 mm), larger root penetration between the joint partners occurred, resulting in a higher value of UL. Additionally, when the welding speed was increased the UL remained almost constant, indicating that the speed was a non-significant process parameter. The optimum value (maximum or minimum) of UL can also be observed from the 3D surface plot. It can be concluded from **Fig. 17** that the maximum values of UL can be achieved at the highest level of beam offset (+0.2 mm) and the lowest level of laser power (331.8 W).

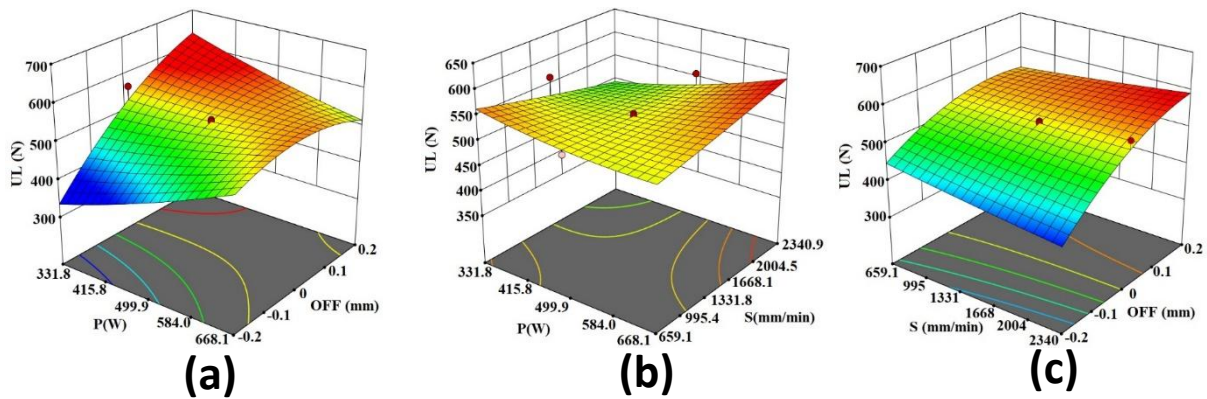


Fig. 17. Response surface plots showing the interaction effects of (a) P and OFF, (b) P and S, (c) S and OFF on the UL, while the third parameter is at their respective centre value

It was observed that both PD (Fig. 18a and b) and WW (Fig. 19a and b) increased with an increase in the value of laser power. Increasing the laser power increases the power density per unit area resulting in a large amount of base metal being melted consequently forming a weld with deeper penetration depth and wider width. In contrast, increasing the welding speed reduces WW. This was because the interaction time decreased with an increase in welding speed and less energy was delivered to the base metal/weld joint. The maximum value for both PD and WW was achieved at -0.2 mm offset and the lowest value of welding speed (Fig. 18c and 19c). Since the laser beam was shifted away from the joint interface with high interaction time and subsequently, the maximum PD and WW were achieved.

It can be observed from Fig. 20 and 21 that the variation in TT and MTT with process parameters are almost similar and therefore the maximum values of TT will be obtained at the highest value of laser power (668.1 W) and the lowest value of the welding speed (659.1 mm/min). Whereas, the maximum value of MTT was achieved at the lowest values of laser power (331.8 W) and the highest value of beam offset (0.2 mm). The significance of process parameters can also be determined from the 3D surface plot. It is evident from Fig. 20 and 21 that beam offset had the most significant effect on TT and MTT followed by laser power and welding speed. Because the alteration in the values of TT and MTT is rapid with changing the values of OFF.

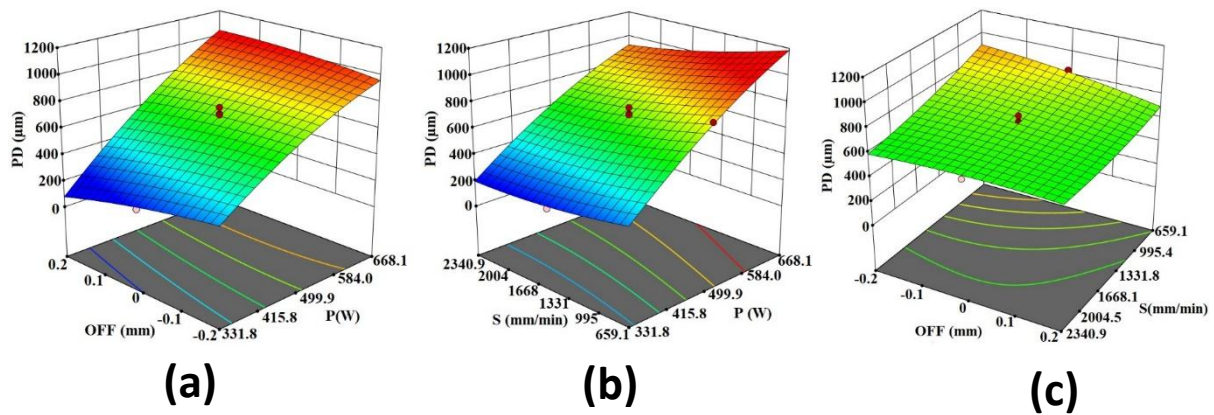


Fig. 18. Response surface plots showing the interaction effects of (a) P and OFF, (b) P and S, (c) S and OFF on the PD, while the third parameter is at their respective centre value

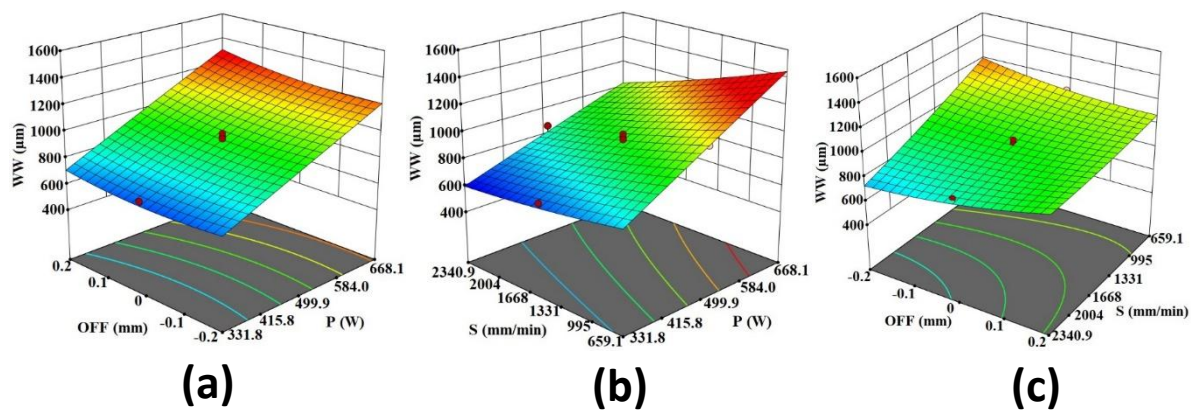


Fig. 19. Response surface plots showing the interaction effects of (a) P and OFF, (b) P and S, (c) S and OFF on the WW, while the third parameter is at their respective centre value

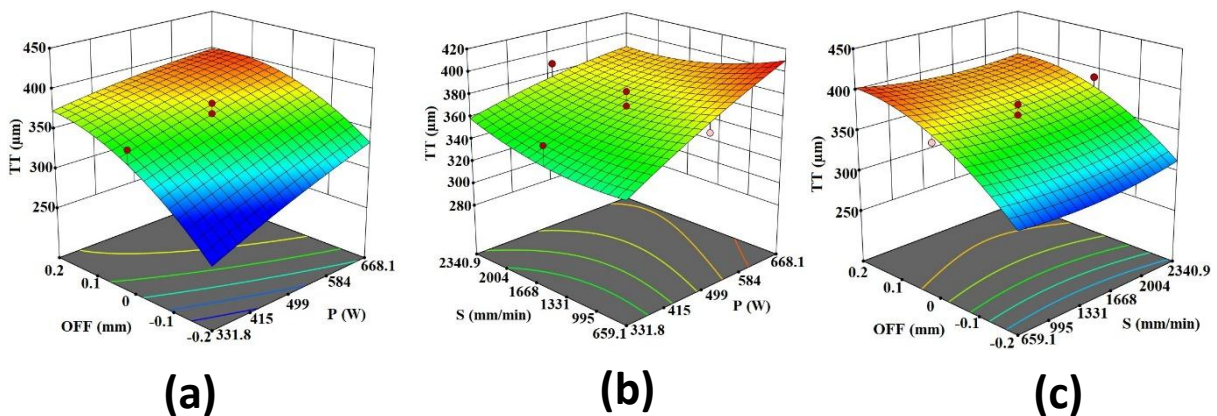


Fig. 20. Response surface plots showing the interaction effects of (a) P and OFF, (b) P and S, (c) S and OFF on the TT, while the third parameter is at their respective centre value

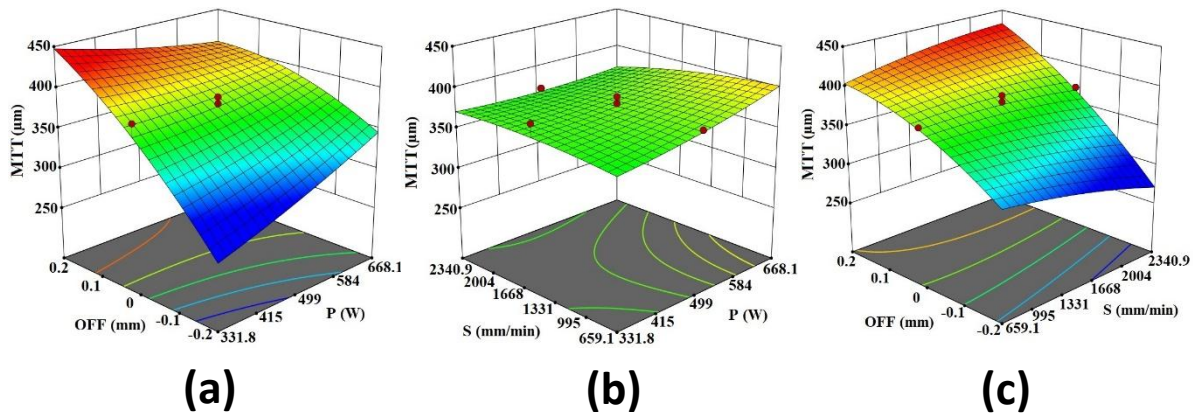


Fig. 21. Response surface plots showing the interaction effects of (a) P and OFF, (b) P and S, (c) S and OFF on the MTT, while the third parameter is at their respective centre value

3.4.5. Correlation between responses

In order to determine the relationship between the responses, a Pearson correlation test was applied for each set of responses. Both the Pearson correlation coefficient (r-value) and statistical significance (p-values) are displayed in **Fig. 22**. Although the relationship between the UL-TT, UL-MTT, WW-PD and MTT-TT show statistical significance ($p < 0.05$) at 95% confidence level, the r-values indicated the linear association between two responses.

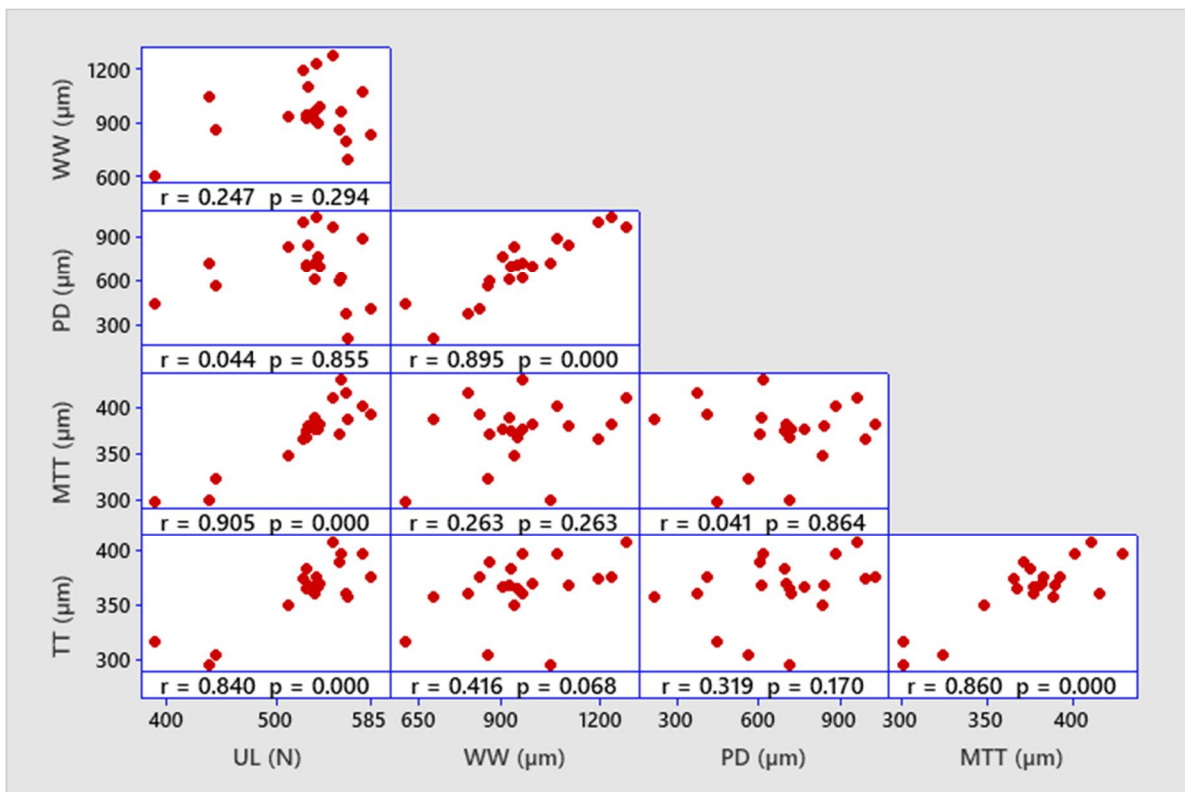


Fig. 22. Pearson correlations (r-value) and statistical significance (p-value) tests between the responses

The r-value can range in value from -1 to +1. For example, r will be +1, when both the variables increase by a consistent amount. If the relationship is that one variable increase when the other increases, but the amount is not consistent, r is positive but less than +1. Similarly, if the relationship is that one variable decrease when the other increases, but the amount is not consistent, then the Pearson correlation coefficient is negative but greater than -1. $r = 0$ indicates no linear correlation between the responses [55]. From **Fig. 22**, it is observed that the highest correlation value ($r = 0.905$) was obtained for the UL-MTT indicating that the ultimate load is highly correlated with the modified throat thickness which signifies the importance of MTT over the other responses associated with bead geometry (i.e., WW, PD and TT). It can also be seen that the UL increased with an increase in the values of MTT with corresponding r-values of 0.905. WW ($r = 0.247$) and PD ($r = 0.044$) have no significant effect on UL. Strong relationships were also obtained between PD-WW and TT-MTT with corresponding r-values of 0.895 and 0.860 respectively.

3.4.6. Optimization using desirability function analysis

Desirability function analysis is one of the most extensively used approaches in industry for the optimization of response/s [6]. Single objective optimization for laser welding of Al was carried out and the optimized results of average maximum load (UL) are shown in **Fig. 23**. The goal was to maximize UL, which is desired for high-quality welds. In order to get the desired response, equal importance has been given to the upper and lower bounds, and the target value of the linear desirability function. For the linear desirability function (d), the value of the weight is considered to be 1 (for each response, a desirability function assigns numbers between 0 and 1; 0 representing a completely undesirable value and 1 representing a completely desirable or ideal response value).

In **Fig. 23**, the row corresponds to a response variable and each column corresponds to one of the process parameters. Each cell of the graph shows how one of the response variables changes as a function of the process parameters, keeping other parameters constant. The vertical line inside the graph indicates the optimum parameter setting and the horizontal dotted line represents the optimized response values. The numbers displayed at the top of the column show the upper and lower limits of process parameters with the optimum parameter level setting (in red). On the left side of the row is shown the goal of the optimisation, the predicted response (y) at the optimum parametric setting, and individual desirability value ($=1$) is given. The optimisation was performed using MINITAB v19. The optimum value of UL (646.89 N) was

obtained at a laser power of 331.82 W, welding speed of 659.10 mm/min and beam offset of 0.2 mm. The value of composite desirability factor (D) was 1 (i.e. the individual desirability was combined using the geometric mean, which gave the overall/composite desirability 'D').

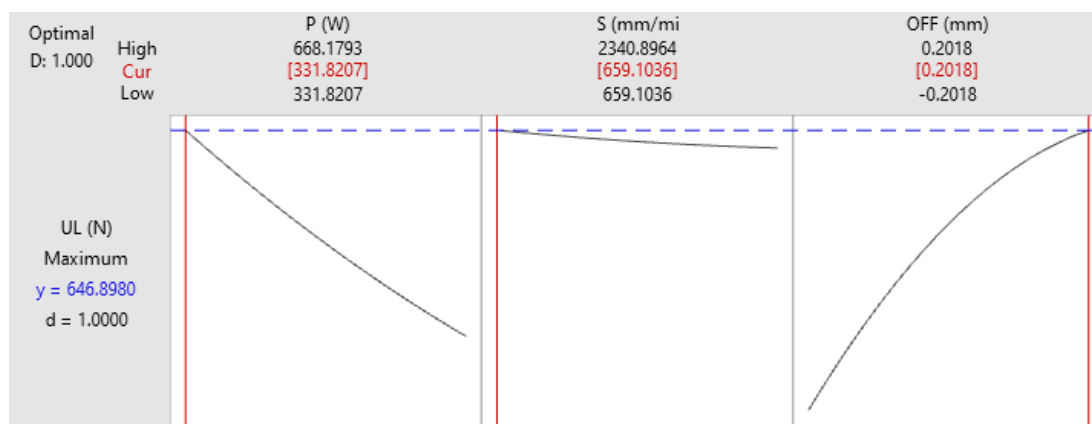


Fig. 23. Optimization results of ultimate load (UL)

3.4.7. Confirmatory experiments

The results of the optimization obtained from the desirability function analysis were validated by conducting confirmatory tests. Three coupon tests were conducted using the optimum parametric settings and the results are presented in **Table 9**. There was only a small percentage between the predicted and the experimental/actual values, which validated the surrogate model and applied optimization method. The measured value of MTT at the optimum welding conditions was greater (455.59 μm) than the obtained MTT values (299.885 μm - 429.487 μm) from CCD design matrix (**Table 7**). A macro and SEM images of the laser-welded sample at the optimum condition is shown in **Fig. 24a** and **b** respectively and the corresponding values of PD, WW and TT were obtained as 396.63 μm , 752.29 μm , 309.82 μm respectively. As shown in **Fig. 24b**, it can be pointed out the grain growth directions were identical to sample no. 6 and 11 from straight and broad columnar grains to fine equiaxed grains than coarse equiaxed grains extended from fusion boundary to the weld center. Also, the trend of micro-hardness profile at the optimum conditions (**Fig. 25**) was identical to sample no. 6 and 11 as well. The micro-hardness profile was measured by entering the fusion zones (FZs) from the lower base metal and leaving the fusion zone to the upper base metal as shown in **Fig. 25**. Micro-hardness of the fusion zones varies from 34.1-39.4 $\text{HV}_{0.025}$ with an average hardness of 36.75 $\text{HV}_{0.025}$ increased slightly (by up to 4%) in comparison with sample no. 6 (i.e., average hardness at FZ= 35.35 $\text{HV}_{0.025}$). Whereas, a significant increment in the MTT value (by about 17%) at the optimum condition weld (455.59 μm) in comparison with sample no. 6 (392.33 μm) may be attributed to more joint strength.

Table 9. Obtained single objective optimization results

| Optimum conditions | | | Response | |
|--------------------|------------|----------|-------------------------------------|---------------------------------|
| P (W) | S (mm/min) | OFF (mm) | UL (N) | |
| 331.80 | 659.10 | 0.20 | Avg. actual Predicted Error% | 602.51 ± 7.58 646.89 6.81 |

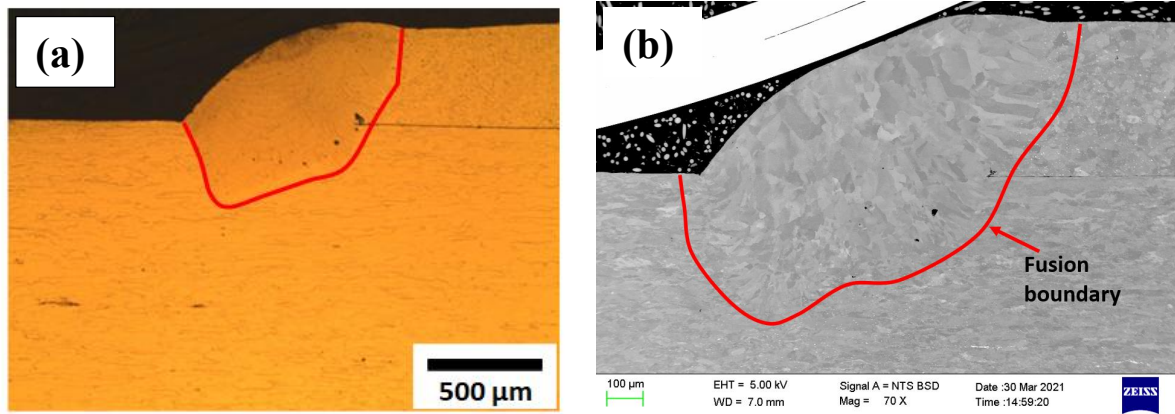


Fig. 24. (a) Macro and (b) SEM images of the sample welding using optimised parameters

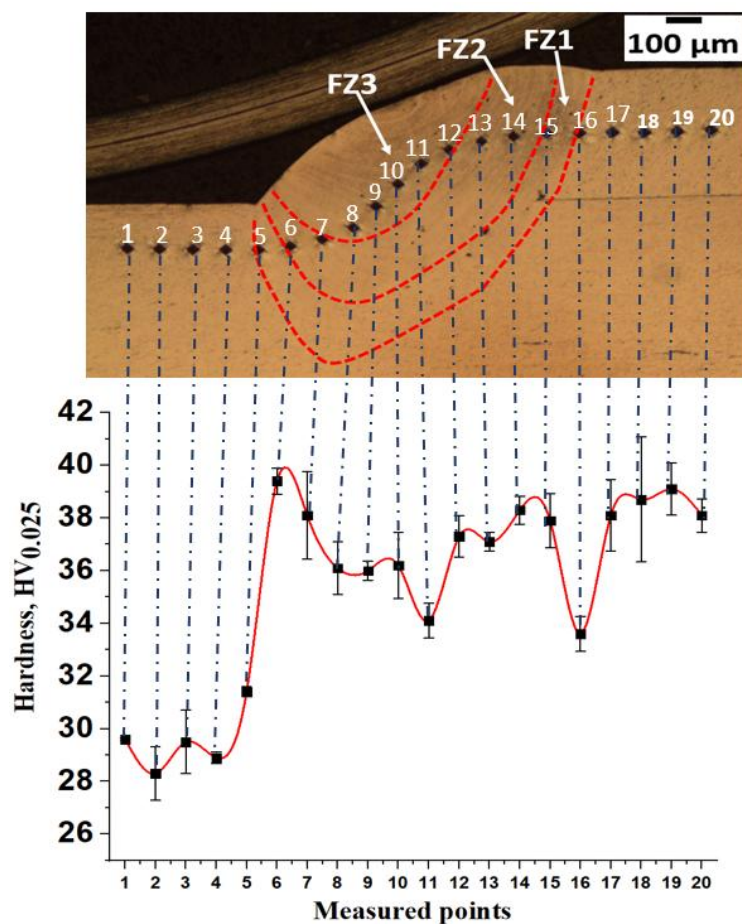


Fig. 25. Microhardness profiles of weld at optimum condition

4. Laser welding of actual geometry (cooling channel and module manifold)

After completing the optimization for laser-welded coupon samples of 0.4 mm Al joined to 1.5 mm Al, the optimized process parameters were used to weld the actual geometry (cooling channel to manifold). A pictorial view of the welded sample is shown in **Fig. 26a** showing two cooling channels successfully welded, and **Fig. 26b** showed a cross-sectional image and micro-hardness profile of the cooling channel and module manifold welding. The measured value of MTT, TT, WW and PD were obtained as 516.07 μm , 364.148 μm , 795.432 μm , 393.16 μm respectively.

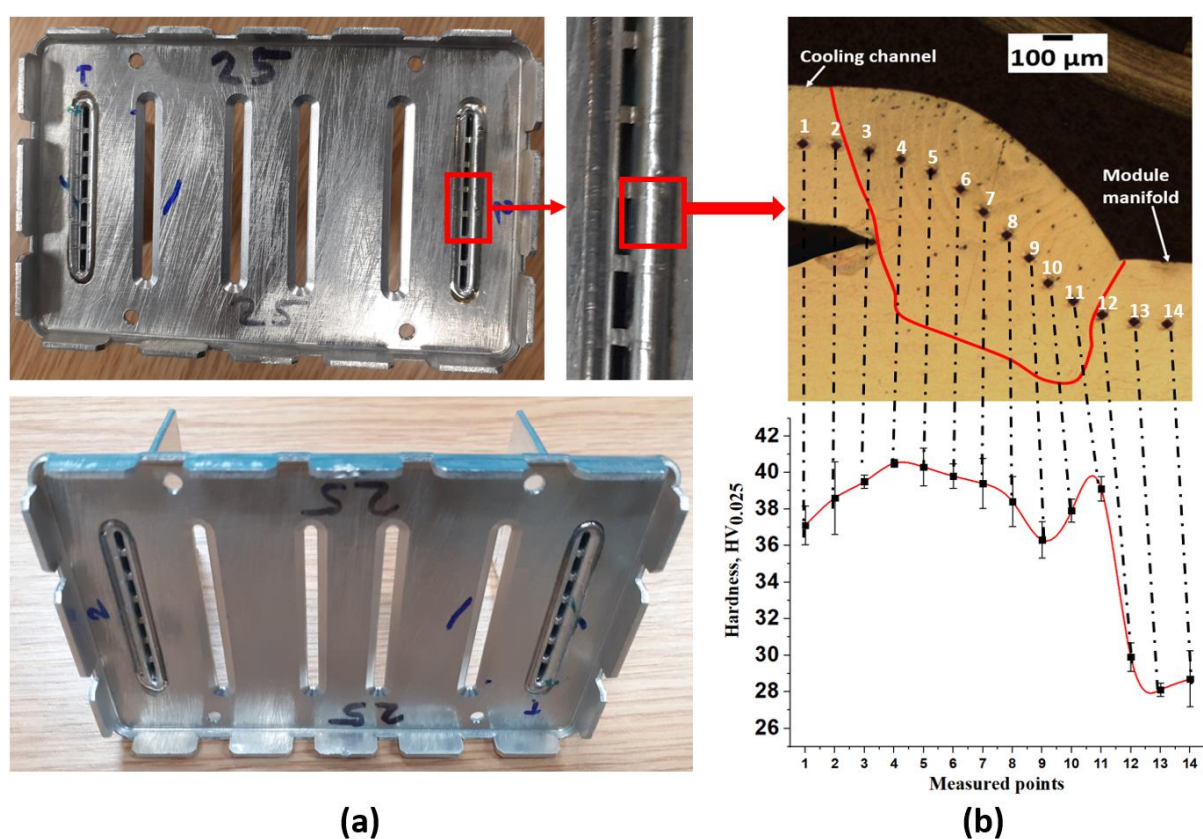


Fig. 26. (a) Laser welding of actual geometry (cooling channel and module manifold) and (b) weld cross-section with micro-hardness profile

The MTT for the actual geometry weld was increased by about 14% than the coupons welding at optimum conditions which is required for the high strength joints. The increment in MTT may be due to a little gap between the cooling channel and the module manifold (see **Fig. 26b**). The micro-hardness profile was measured by entering the fusion zone (FZ) from the cooling channel and leaving the fusion zone to the module manifold as shown in **Fig. 26b**. The maximum micro-hardness was measured as 40.5 HV_{0.025} with an average hardness of 37.4

HV_{0.025} across the fusion zone increased slightly (by up to 1.5%) in comparison with coupons welding (36.75 HV_{0.025}) at optimum condition. It can be concluded that the trend in the microhardness profiles and values are alike among the four welding conditions (i.e. sample no. 6, sample no. 11, optimum condition weld for coupons and actual geometry). It is also evident from the MTT value and micro-hardness profiles that high strength joints would have been achieved for cooling channel to module manifold parts.

5. Conclusions and future work

This paper presented a comprehensive study on laser welding to produce thin-to-thick joints by satisfying the mechanical and metallurgical characteristics. The optimised process parameters were used to join the cooling channel with module manifold of battery thermal management system. From the foregoing analysis and discussion, the following conclusions were drawn:

- Laser wobbling has been demonstrated as a viable technique for joining the cooling channel and the module manifold in the battery cooling system.
- The heat input (line energy) is not a convenient method to parameterize the laser beam welding parameters.
- The average microhardness values of the fusion zones (up to 35.6 HV_{0.025}) were within the average microhardness values of upper (38.6 HV_{0.025}) and lower base (29.5 HV_{0.025}) materials which signify that good-weld can be achieved using laser wobble joining.
- EBSD maps confirmed that sample with higher HAGB from the fusion zone resulted in a higher ultimate load. It was obtained that the sample having the highest tensile load of 584.84 N showed around a 20% increase in HAGB in comparison to the sample having the lowest ultimate load (i.e. 390.46 N).
- From ANOVA analysis, it was found that the laser beam offset had the most significant influence on the responses such as ultimate load, throat thickness and modified throat. This signified the importance of laser beam offset for producing the high strength fillet edge weld.
- The optimized process parameters for the ultimate load (maximization) was evaluated by desirability function analysis and the result of the obtained parametric combination (laser power at 331.80 W, welding speed at 659.10 mm/min and offset at 0.2 mm) was verified by confirmatory experiment.

N. Kumar, A. Das, T. Dale, I. Masters, *Laser wobble welding of fluid-based cooling channel joining for battery thermal management*, **Journal of Manufacturing Processes**, 67 (2021) 151-169.

A systematic study was conducted in this work to optimise the laser welding process parameters for fluid channel welding of battery cells. Further, the optimised welded joints can be used for thermal characterisation as future work. In addition, corrosion analyses may be conducted for the welded samples.

Acknowledgements

This research work is supported by the Innovate UK Faraday Battery Challenge (grant no.133864) through the WMG Centre High Value Manufacturing (HVM) Catapult, The University of Warwick in collaboration with Heat Trace Limited and Nobel Automotive U.K. Limited.

References

- [1] A. Das, D. Li, D. Williams, D. Greenwood, Joining Technologies for Automotive Battery Systems Manufacturing, *World Electric Vehicle Journal* 9(2) (2018) 22.
- [2] M.J. Brand, P.A. Schmidt, M.F. Zaeh, A. Jossen, Welding techniques for battery cells and resulting electrical contact resistances, *Journal of Energy Storage* 1 (2015) 7-14.
- [3] P.A. Schmidt, M. Schweier, M.F. Zaeh, Joining of lithium-ion batteries using laser beam welding: Electrical losses of welded aluminum and copper joints, *International Congress on Applications of Lasers & Electro-Optics* 2012(1) (2012) 915-923.
- [4] D. Chen, J. Jiang, G.-H. Kim, C. Yang, A. Pesaran, Comparison of different cooling methods for lithium ion battery cells, *Applied Thermal Engineering* 94 (2016) 846-854.
- [5] S. Wang, Y. Li, Y.-Z. Li, Y. Mao, Y. Zhang, W. Guo, M. Zhong, A forced gas cooling circle packaging with liquid cooling plate for the thermal management of Li-ion batteries under space environment, *Applied Thermal Engineering* 123 (2017) 929-939.
- [6] N. Kumar, M. Mukherjee, A. Bandyopadhyay, Study on laser welding of austenitic stainless steel by varying incident angle of pulsed laser beam, *Optics & Laser Technology* 94 (2017) 296-309.
- [7] C. Brock, R. Hohenstein, M. Schmidt, Mechanisms of vapour plume formation in laser deep penetration welding, *Optics and Lasers in Engineering* 58 (2014) 93-101.
- [8] M. Kraetzsch, J. Standfuss, A. Klotzbach, J. Kaspar, B. Brenner, E. Beyer, Laser Beam Welding with High-Frequency Beam Oscillation: Welding of Dissimilar Materials with Brilliant Fiber Lasers, *Physics Procedia* 12 (2011) 142-149.
- [9] A. Das, T. Dale, I. Masters, D. Widanage, Feasibility of fillet edge weld using laser wobble technique, *Procedia CIRP* 95 (2020) 846-851.
- [10] G. Shannon, H. Chen, Laser welding of aluminum and copper for battery welding applications using a 500W single mode fiber laser, *International Congress on Applications of Lasers & Electro-Optics* 2009(1) (2009) 1015-1020.
- [11] Y. Deng, C. Feng, J. E, H. Zhu, J. Chen, M. Wen, H. Yin, Effects of different coolants and cooling strategies on the cooling performance of the power lithium ion battery system: A review, *Applied Thermal Engineering* 142 (2018) 10-29.
- [12] M.S. Patil, S. Panchal, N. Kim, M.-Y. Lee, Cooling performance characteristics of 20 Ah lithium-ion pouch cell with cold plates along both surfaces, *Energies* 11(10) (2018) 2550.

- [13] B. Ye, M.R.H. Rubel, H. Li, Design and optimization of cooling plate for battery module of an electric vehicle, *Applied Sciences* 9(4) (2019) 754.
- [14] C. Lan, J. Xu, Y. Qiao, Y. Ma, Thermal management for high power lithium-ion battery by minichannel aluminum tubes, *Applied Thermal Engineering* 101 (2016) 284-292.
- [15] D.S. Buck, R.N. Fattig, B.J. Silk, Battery pack with integral cooling and bussing devices, EnerDel Inc, USA, 2007.
- [16] Y. Kuruma, S. Inoue, Battery Pack, Toyota Jidosha Kabushiki Kaisha, Japan, 2006.
- [17] A. Chu, Y. Yuan, J. Zhu, X. Lu, C. Zhou, The Design and Investigation of a Cooling System for a High Power Ni-MH Battery Pack in Hybrid Electric Vehicles, *Applied Sciences* 10(5) (2020) 1660.
- [18] K. Tagawa, R.J. Brodd, Production Processes for Fabrication of Lithium-Ion Batteries, in: M. Yoshio, R.J. Brodd, A. Kozawa (Eds.), *Lithium-Ion Batteries: Science and Technologies*, Springer New York, New York, NY, 2009, pp. 181-194.
- [19] G. Berdichevsky, K. Kelty, J. Straubel, E. Toomre, The tesla roadster battery system, (2006).
- [20] A. Das, A. Barai, I. Masters, D. Williams, Comparison of tab-to-busbar ultrasonic joints for electric vehicle Li-ion battery applications, *World Electric Vehicle Journal* 10(3) (2019) 55.
- [21] A. Das, D. Li, D. Williams, D. Greenwood, Weldability and shear strength feasibility study for automotive electric vehicle battery tab interconnects, *Journal of the Brazilian Society of Mechanical Sciences and Engineering* 41(1) (2019) 54.
- [22] S. Shawn Lee, T. Hyung Kim, S. Jack Hu, W.W. Cai, J.A. Abell, J. Li, Characterization of Joint Quality in Ultrasonic Welding of Battery Tabs, *Journal of Manufacturing Science and Engineering* 135(2) (2013) 021004-13.
- [23] S. Dhara, A. Das, Impact of ultrasonic welding on multi-layered Al-Cu joint for electric vehicle battery applications: A layer-wise microstructural analysis, *Materials Science and Engineering: A* 791 (2020) 139795.
- [24] G. Reinhart, T. Zeilinger, J. Kurfer, M. Westermeier, C. Thiemann, M. Glonegger, M. Wunderer, C. Tammer, M. Schweier, M. Heinz, Research and Demonstration Center for the Production of Large-Area Lithium-Ion Cells, (2013) 3-12.
- [25] S. Das, M.P. Satpathy, B.C. Routara, S.K. Sahoo, S. Gantayat, Mechanical Behavior of Ultrasonic Spot Welded Aluminum to Cupro-Nickel Sheets for Battery Tabs, *IOP Conference Series: Materials Science and Engineering*, IOP Publishing, 2019, p. 012031.
- [26] Z. Ma, Y. Zhang, The Effect of Ultrasonic Energy on Joint Characterization in Ultrasonic Spot Welding Multilayer Tabs Used in Lithium-Ion Battery Manufacturing, *MATEC Web of Conferences*, EDP Sciences, 2019, p. 02003.
- [27] D. Walter, B. Schmieder, V.R. Moldovan, Nothing Less Than More Affordable Lithium-Ion Batteries: A new laser welding process as an even smarter way of making bonds, *Laser Technik Journal* 11(4) (2014) 44-47.
- [28] G. Shannon, Improve Tab to Terminal Connections in Battery Pack Manufacturing, 2016.
- [29] U.F. Shaikh, A. Das, A. Barai, I. Masters, Electro-Thermo-Mechanical Behaviours of Laser Joints for Electric Vehicle Battery Interconnects, 2019 Electric Vehicles International Conference (EV), IEEE, 2019, pp. 1-6.
- [30] S. Dong, G. Kelkar, Y. Zhou, Electrode sticking during micro-resistance welding of thin metal sheets, *IEEE transactions on electronics packaging manufacturing* 25(4) (2002) 355-361.
- [31] A. Das, R. Fritz, M. Finuf, I. Masters, Blue laser welding of multi-layered AISI 316L stainless steel micro-foils, *Optics & Laser Technology* 132 (2020) 106498.

N. Kumar, A. Das, T. Dale, I. Masters, *Laser wobble welding of fluid-based cooling channel joining for battery thermal management*, **Journal of Manufacturing Processes**, 67 (2021) 151-169.

- [32] T. Sun, P. Franciosa, M. Sokolov, D. Ceglarek, Challenges and opportunities in laser welding of 6xxx high strength aluminium extrusions in automotive battery tray construction, *Procedia CIRP* 94 (2020) 565-570.
- [33] A. Das, R. Beaumont, I. Butterworth, I. Masters, D. Williams, High rate and temperature-dependent tensile characterisation with modelling for gap-bridged remote laser welded (RLW) joint using automotive AA5182 alloy, *International Journal of Impact Engineering* 144 (2020) 103672.
- [34] N. Kumar, R. Sherlock, D. Tormey, Prediction of Weld Interface Depth and Width at Optimum Laser Welding Temperature for Polypropylene, *Procedia CIRP* 81 (2019) 1272-1277.
- [35] A. Das, I. Butterworth, I. Masters, D. Williams, Evaluation of Key Geometrical and Mechanical Properties for Remote Laser Welded AC-170PX Aluminium Joints, *Journal of Laser Micro/Nanoengineering* 14(1) (2019) 1-7.
- [36] A. Das, I. Masters, D. Williams, Understanding novel gap-bridged remote laser welded (RLW) joints for automotive high-rate and temperature applications, *International Journal of Mechanical Sciences* 190 (2021) 106043.
- [37] I. Tomashchuk, D. Grevey, P. Sallamand, Dissimilar laser welding of AISI 316L stainless steel to Ti6–Al4–6V alloy via pure vanadium interlayer, *Materials Science and Engineering: A* 622 (2015) 37-45.
- [38] M. Ishak, K. Yamasaki, K. Maekawa, Lap fillet welding of thin sheet AZ31 magnesium alloy with pulsed Nd:YAG laser, *Journal of Solid Mechanics and Materials Engineering* 3 (2009) 1045-1056.
- [39] H.M. Westergaard, Bearing Pressures and Cracks, *Journal of Applied Mechanics* 6 (1939) 49-53.
- [40] SmithMetal. <https://www.smithmetal.com/1050a.htm>. (Accessed 22-11-2019).
- [41] A. Das, I. Butterworth, I. Masters, D. Williams, Microstructure and mechanical properties of gap-bridged remote laser welded (RLW) automotive grade AA 5182 joints, *Materials Characterization* 145 (2018) 697-712.
- [42] M. Sokolov, A. Salminen, Methods for Improving Laser Beam Welding Efficiency, *Physics Procedia* 56 (2014) 450-457.
- [43] R. Sołtysiak, T. Giętka, A. Sołtysiak, The effect of laser welding power on the properties of the joint made of 1.4462 duplex stainless steel, *Advances in Mechanical Engineering* 10(1) (2018) 1687814017751949.
- [44] S. Datta, M.S. Raza, P. Saha, D.K. Pratihari, Effects of Line Energy on Mechanical Properties, Corrosion and Shape Memory Behavior of Laser-Welded NiTiNol Joints, *ASME 2018 13th International Manufacturing Science and Engineering Conference*, 2018.
- [45] S. Kou, *Welding metallurgy*, John Wiley & Sons, New Jersey, USA, 2003.
- [46] M.E. Kassner, The Effect of Low-Angle and High-Angle Grain Boundaries on Elevated Temperature Strength, *MRS Proceedings* 362 (1994) 157.
- [47] S.V.S. Narayana Murty, S. Torizuka, K. Nagai, T. Kitai, Y. Kogo, Effects of strain on grain boundary characteristics and their correlation to mechanical properties in low carbon steel processed by warm multipass calibre rolling, *Materials Science and Technology* 24(10) (2013) 1167-1173.
- [48] Y.J. Li, L. Arnberg, Solidification structures and phase selection of iron-bearing eutectic particles in a DC-cast AA5182 alloy, *Acta Materialia* 52(9) (2004) 2673-2681.
- [49] J. Frostevarg, Factors affecting weld root morphology in laser keyhole welding, *Optics and Lasers in Engineering* 101 (2018) 89-98.
- [50] T. Forsman, *Laser welding of aluminium alloys*, Luleå tekniska universitet, 2000.

N. Kumar, A. Das, T. Dale, I. Masters, *Laser wobble welding of fluid-based cooling channel joining for battery thermal management*, **Journal of Manufacturing Processes**, 67 (2021) 151-169.

- [51] C. Hagenlocher, P. Stritt, R. Weber, T. Graf, Strain signatures associated to the formation of hot cracks during laser beam welding of aluminum alloys, *Optics and Lasers in Engineering* 100 (2018) 131-140.
- [52] D.C. Montgomery, *Design and analysis of experiments*, John Wiley & sons 2017.
- [53] O. Grong, *Metallurgical Modelling of Welding*, The Institute of Materials, Cambridge University Press, UK, 1997.
- [54] W.J. Suder, S.W. Williams, Investigation of the effects of basic laser material interaction parameters in laser welding, *Journal of Laser Applications* 24(3) (2012) 032009.
- [55] J. Benesty, J. Chen, Y. Huang, I. Cohen, Pearson Correlation Coefficient, in: I. Cohen, Y. Huang, J. Chen, J. Benesty (Eds.), *Noise Reduction in Speech Processing*, Springer Berlin Heidelberg, Berlin, Heidelberg, 2009, pp. 1-4.
- [56] L.H. Shah, F. Khodabakhshi, A. Gerlich, Effect of beam wobbling on laser welding of aluminum and magnesium alloy with nickel interlayer, *Journal of Manufacturing Process* 37 (2019) 212-219.
- [57] F. Khodabakhshi, L.H. Shah, A.P. Gerlich, Dissimilar laser welding of an AA6022-AZ31 lap-joint by using Ni-interlayer: Novel beam-wobbling technique, processing parameters, and metallurgical characterization, *Optics and Laser Technology* 112 (2019) 349-362.
- [58] H. Tasalloti, P. Kah, J. Martikainen, Laser overlap welding of Zn-Coated steel on aluminium alloy for patchwork blank applications in the automotive industry, *Reviews on Advanced Materials Science* 40 (2015) 295–302.
- [59] K. Oussaid, A. El Ouafi, A. Chebak, Experimental investigation of laser welding process in overlap joint configuration, *Chemistry of Materials* 7 (2019) 16–31.
- [60] M. Masoumi, S.P.H. Marashi, M. Pouranvari, Metallurgical and mechanical characterization of laser spot welded low carbon steel sheets, *Materials Technology* 81 (2010) 1144–1150.
- [61] S. Meco, S. Ganguly, S. Williams, N. McPherson, Design of laser welding applied to T joints between steel and aluminium, *Journal of Materials Processing Technology* 268 (2019) 132–139.
- [62] J. Enz, V. Khomenko, S. Riekehr, V. Ventzke, N. Huber, N. Kashaev, Single-sided laser beam welding of adissimilar AA2024–AA7050 T-joint. *Materials & Design* 76 (2015) 110–116.
- [63] N. Kumar, M. Mukherjee, A. Bandyopadhyay, Comparative study of pulsed Nd:YAG laser welding of AISI 304 and AISI 316 stainless steels, *Optics & Laser Technology* 88 (2017) 24-39.
- [64] T. Csanádi, M. Bl'anda, N.Q. Chinh, P. Hvizdoš, J. Dusza, Orientation-dependent hardness and nanoindentation-induced deformation mechanisms of WC crystals, *Acta Materialia* 83 (2015) 397–407.
- [65] Y. Yuan, J. Zhang, T. Sun, C. Liu, Y. Geng, Y. Yan, P. Jin, Crystallographic orientation-dependent pattern replication in direct imprint of aluminum nanostructures, *Nanoscale Research Letters* 10 (2015) 96.